Coronal Magnetic Fields – on modeling and observations

Yihua YAN
Key Laboratory of Solar Activity
National Astronomical Observatories
Chinese Academy of Sciences
Beijing 100012, China

Outline

I. Introduction
II. Coronal Field Reconstructions
III. Radio Capabilities for Imaging Spectroscopic Observations
IV. Summary

Introduction

Coronal magnetic fields are mainly inferred from:

- Numerical reconstruction from reliable bottom boundary magnetograms
- IR measurement by Zeeman effect
- EUV/UV measurement by Hanle effect
- Radio diagnosis due to different emission mechanism
- Structure as revealed in SXR, UV/EUV images, etc.

Here we introduce some recent work on:

- Reconstructed NLFFF results as compared with 3D structures inferred from EUV observations by DBIE (Wang, Yan, Tan, 2013, Sol. Phys. v.288, pp. 507-529)
- Tracking back solar wind to its photospheric footpoints (Huang,Yan,Li, et al. Sol. Phys.,2014, in press)
- Progress on Chinese Spectral Radioheliograph (CSRH) in 400MHz-15GHz range with >500 frequency channels (Yan et al. Earth Moon & Planets, 2009; Wang, Yan, Liu et al. PASJ, 2013, …)

Coronal Loops:

Those loop or thread-like structures are believed to resemble the coronal magnetic field.

However, what we observe are plasmas, not magnetic field !

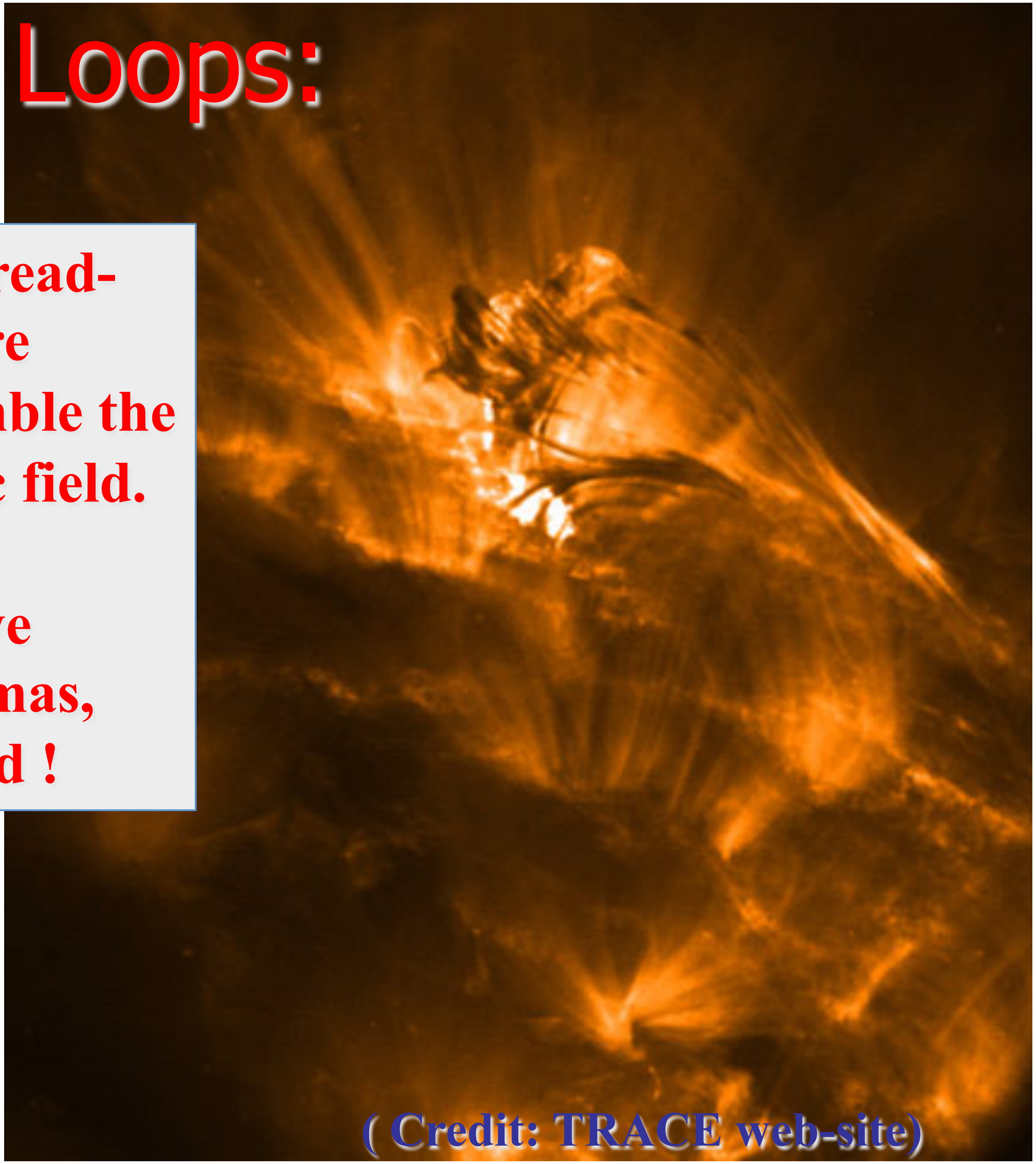

(Credit: TRACE web-site)

Coronal Loops:

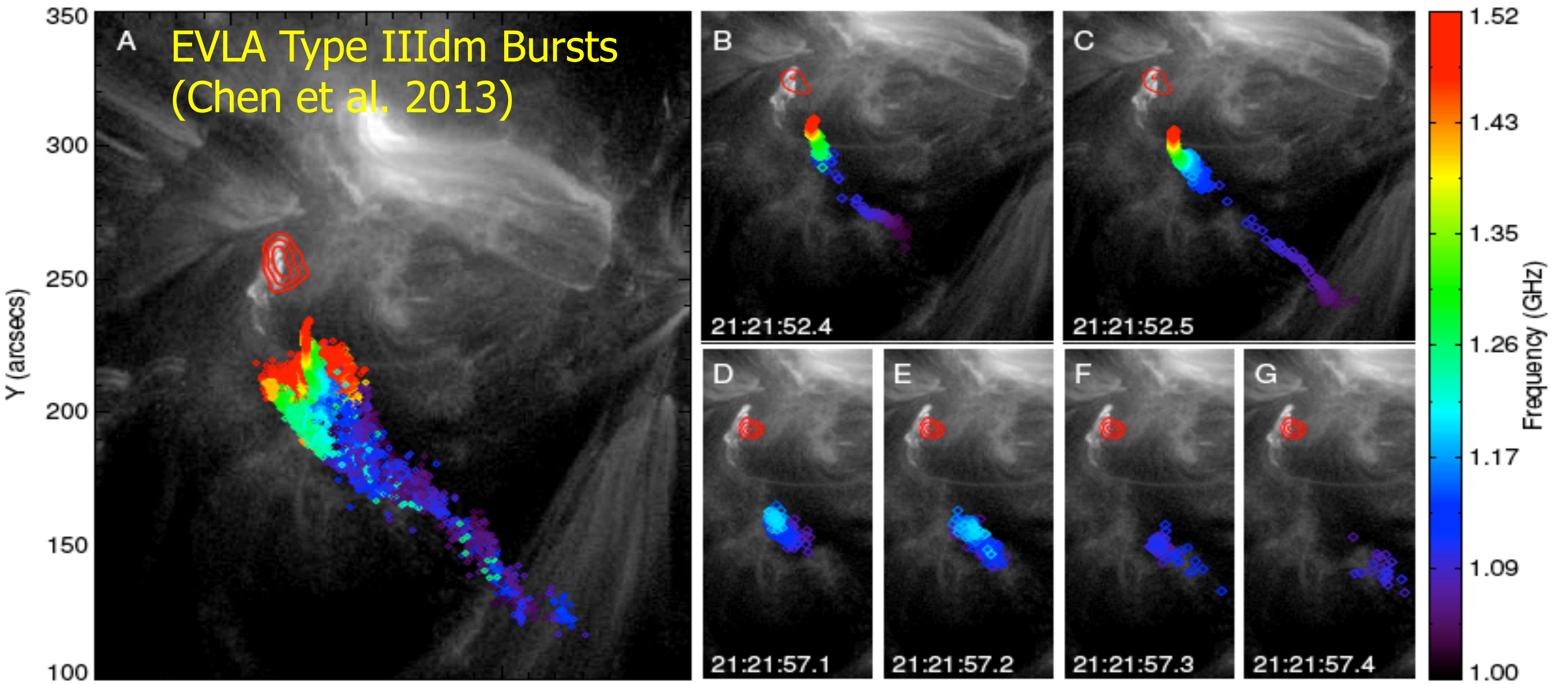

Type IIIdm electron beams should be along cooler & over-denser coronal "fibrous" magnetic loops that are composed of unresolved "strands" and invisible in EUV images (Chen et al. 2013).

⇒One has to reconstruct the coronal magnetic field

(Credit: TRACE web-site)

On NLFFF modeling

- **Many efforts available for NLFFF (Sakurai 1981, Wu et al. 1990; Mikic et al 1995; Yan & Sakurai 1997,2000; Amari et al. 1999; Wheatland et al. 2000; Wiegelmann 2004; Valori et al. 2005; Yan & Li 2006; Hu et al. 2008; ...), but also non-FFF efforts**
- **The BIE/DBIE representation of the NLFFF:**
  1. **assume finite energy content in semi-space**
  2. **do not need arbitrarily-prescribed lateral and top boundary data**
  3. **use bottom boundary vector B**
  4. **over-determine the NLFFF as some other models**

The DBIE model (Yan & Li, 2006, ApJ): With given λ's

$$B_p(x_i, y_i, z_i) = \int_\Gamma \frac{z_i[\lambda_{pi} r \sin(\lambda_{pi} r) + \cos(\lambda_{pi} r)] B_{p0}(x, y, 0)}{2\pi[(x - x_i)^2 + (y - y_i)^2 + z_i^2]^{3/2}} dxdy$$

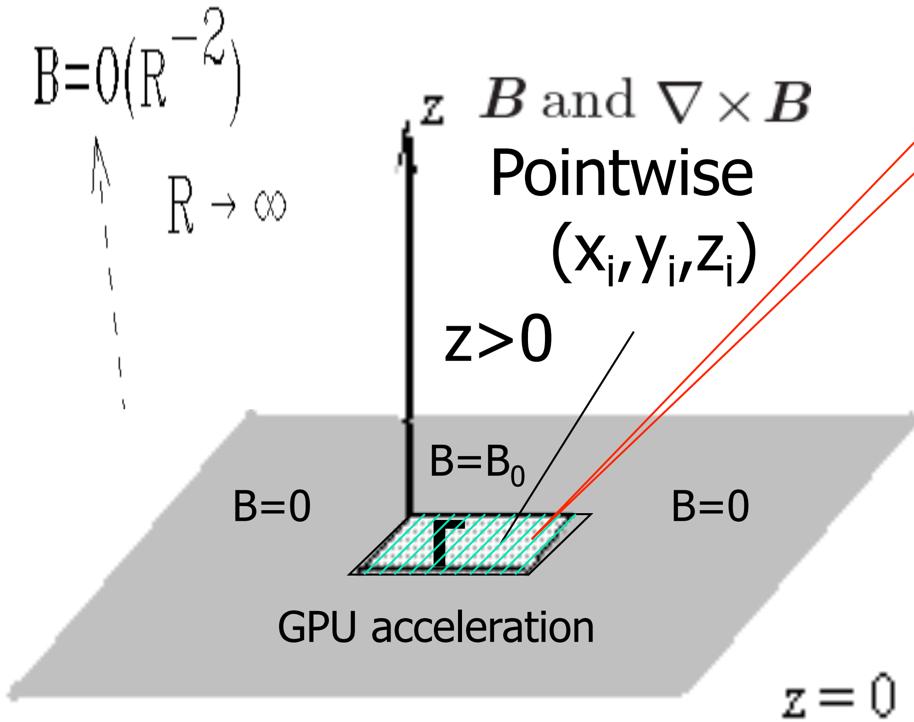

The DBIE model (Yan & Li, 2006, ApJ): With given λ's

$$B_p(x_i, y_i, z_i) = \int_\Gamma \frac{z_i[\lambda_{pi} r \sin(\lambda_{pi} r) + \cos(\lambda_{pi} r)] B_{p0}(x, y, 0)}{2\pi[(x - x_i)^2 + (y - y_i)^2 + z_i^2]^{3/2}} dx dy$$

$$\lambda_p(r) = \lambda_p(r_i) + \lambda_p{}'(\xi)(r - r_i)$$

$$\lambda_p(r) \approx \lambda_p(r_i)$$

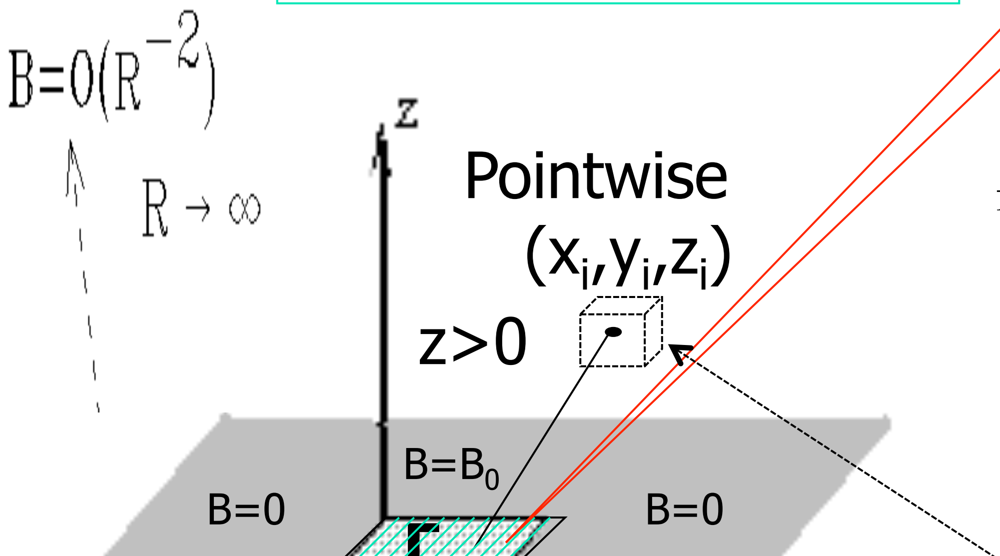

Like Mont Carlo method, modify λ's by a downhill method from minimizing:

- force-freeness

$$f_i(\lambda_x, \lambda_y, \lambda_z) = \frac{|\mathbf{J} \times \mathbf{B}|}{|\mathbf{J}||\mathbf{B}|}, \text{ with } \mathbf{J} = \nabla \times \mathbf{B}$$

- divergence-free by relative flux error

$$g_i(\lambda_x, \lambda_y, \lambda_z) = \frac{|\delta \mathbf{B}_i|}{|\mathbf{B}_i|} = \frac{|\nabla \bullet \mathbf{B}| \Delta V_i}{|\mathbf{B}| \Delta \sigma_i}$$

ΔV_i --- a small neighborhood (~0.001 pixel size) volume;
$\Delta \sigma_i$ --- the surface area

A practical and rigorous numerical procedure as opposite to some comment about it. (Wang, Yan & Tan, Solar Physics, 2013)

Table 1. Evaluation of metrics for the present DBIE and other methods.

Only lower boundary provided, entire volume[1]	C_{vec}	C_{cs}	E'_n	E'_m	ϵ
Exact solution (Low & Lou, 1990)	1	1	1	1	1
Weighted Optimization Method (Wiegelmann)[2]	1.00	0.57	0.86	-0.25	1.04
Optimization Method (McTiernan)[2]	1.00	0.51	0.84	-0.38	1.04
Magnetofrictional Method (Valori)[2]	0.99	0.55	0.75	-0.15	1.02
Grad - Rubin - like Method (Wheatland)[2]	0.99	0.58	0.69	0.13	0.96
Grad - Rubin - like Method (Régnier)[2]	0.94	0.28	0.49	-1.7	0.74
Boundary Integral Method (no iteration)[2]	0.97	0.41	-0.02	-14.	1.00
Upward-layered DBIE Method (He)[3]	0.97	0.65	0.077	12.4	1.06
Present DBIE Method	0.99	0.52	0.83	-0.53	1.08

[1]The parameters are the same as in Case II in Schrijver et al. (2006) with Low & Lou (1990) solution: n=3, m=1, l=0.3, $\Phi = 4\pi/5$ on a 192×192 pixel grid centered on the $64 \times 64 \times 64$-pixel test region.
[2]Data from Table I of Schrijver et al. (2006).
[3]Data from Table 4 of He & Wang (2008).

For a test case, the metrics significantly improved as compared with BIE without iteration ; and similar results as compared with other NLFFF methods (Wang, Yan & Tan, Solar Physics, 2013)

An X2.2 flare in NOAA 11158 at 01:44 UT on 15 Feb 2011 (Schrijver et al., 2011; Sun et al., 2012; Wiegelmann et al., 2012; Jing et al., 2012; Vemareddy et al., 2012; Song et al., 2013;…). Most studies have the aid of extrapolation methods, but none have demonstrated the 3-D view as compared with SDO & STEREO A/B observations

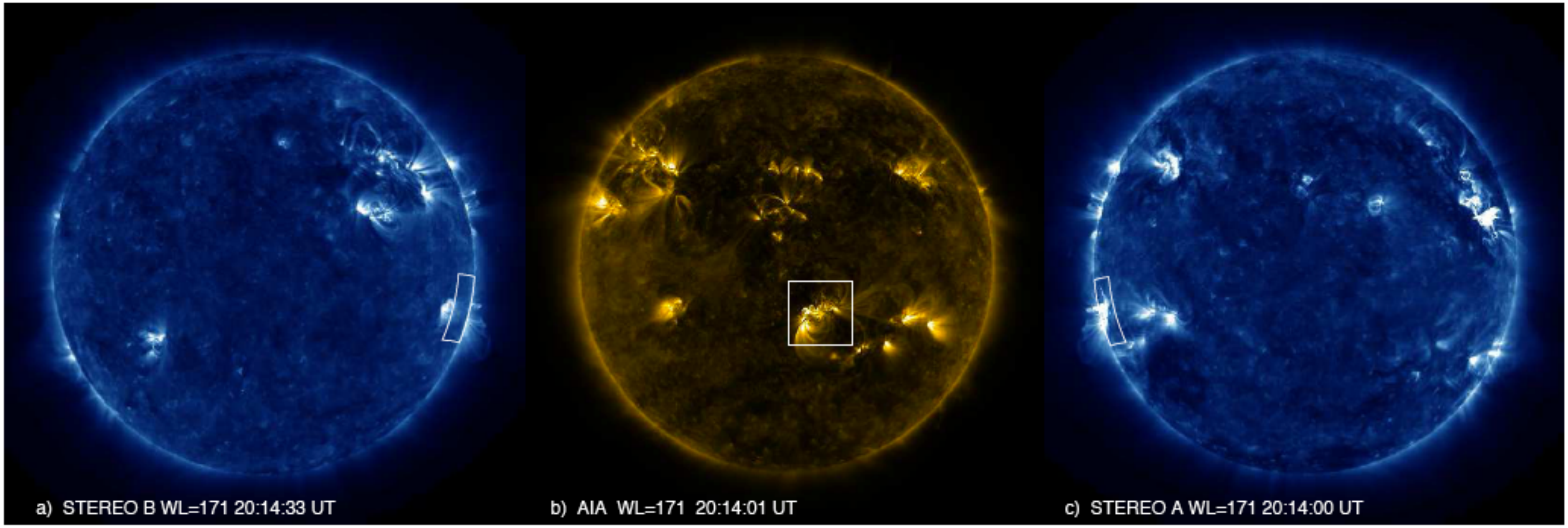

The 180◦ ambiguity and the boundary data are processed (Wang et al. 2001) but no preprocessing to remove non-force-freeness.

An X2.2 flare :44 UT on 15 Feb 2011 (Schrijver 2; Wiegelmann et al., 2012; Jing et al., .2; Song et al., 2013;…). Most studies polation methods, but none hav 3-D view as compared wi B observations

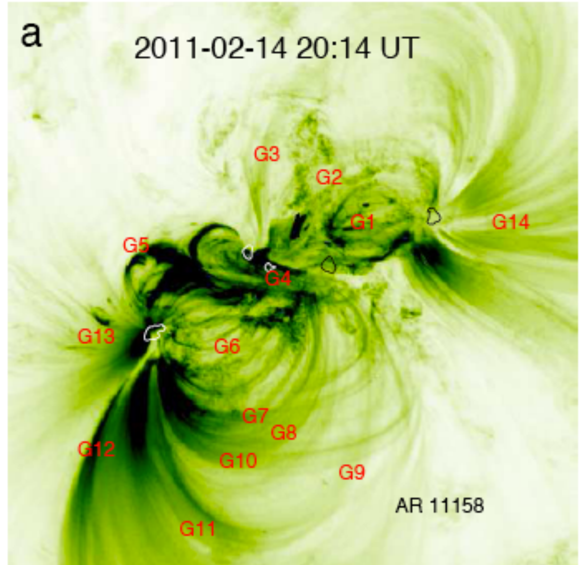

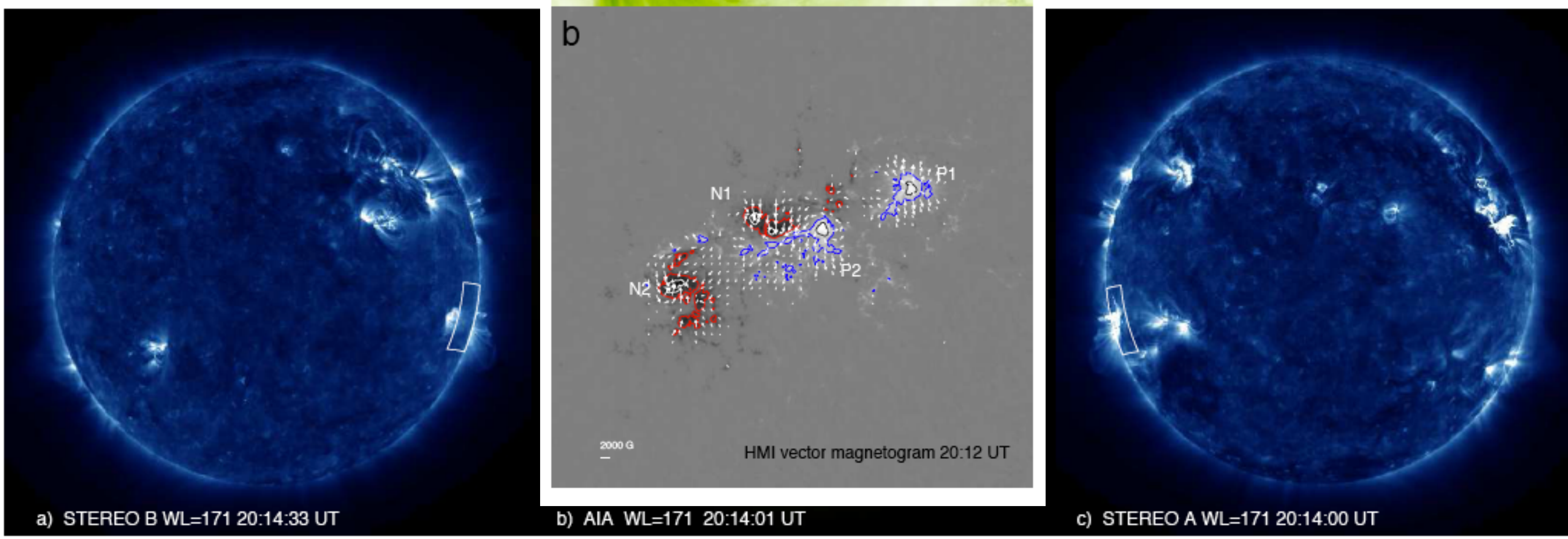

The 180◦ ambiguity and the boundary data are processed (Wang et al. 2001) but no preprocessing to remove non-force-freeness.

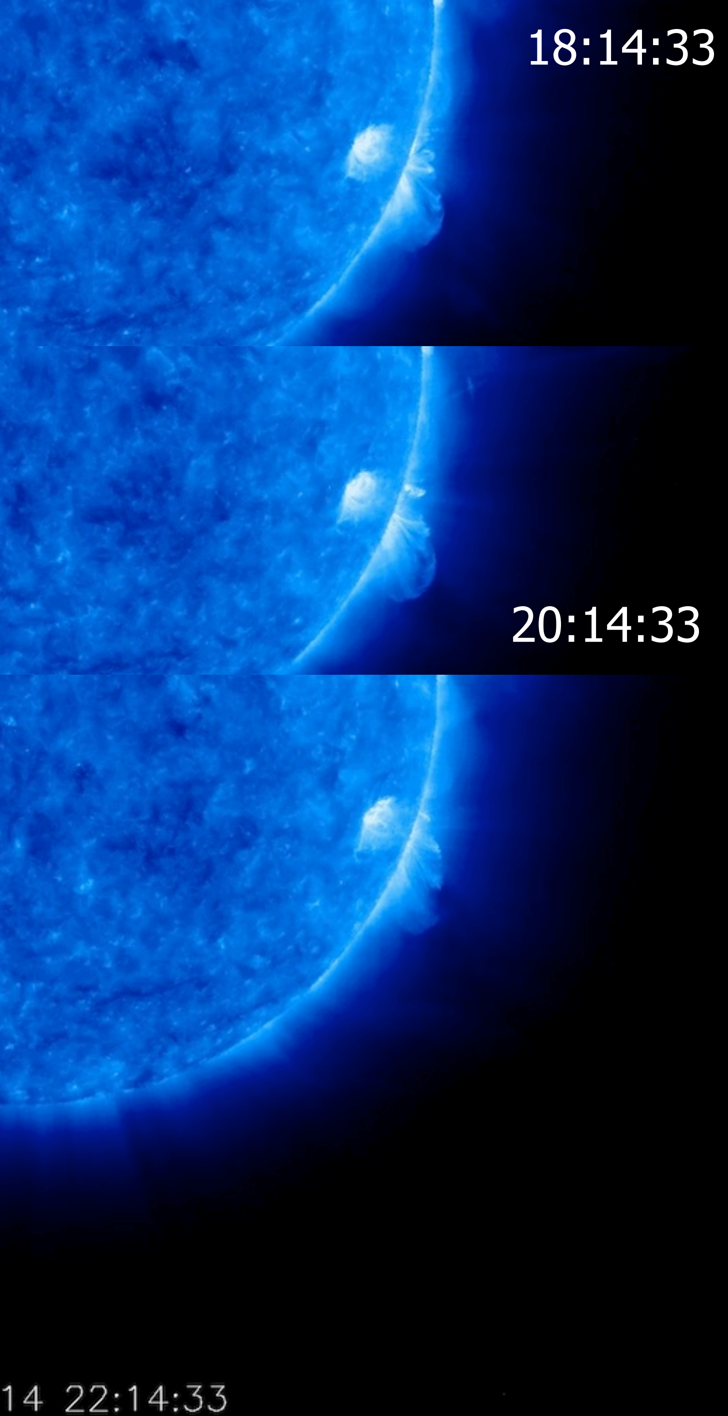

STEREO

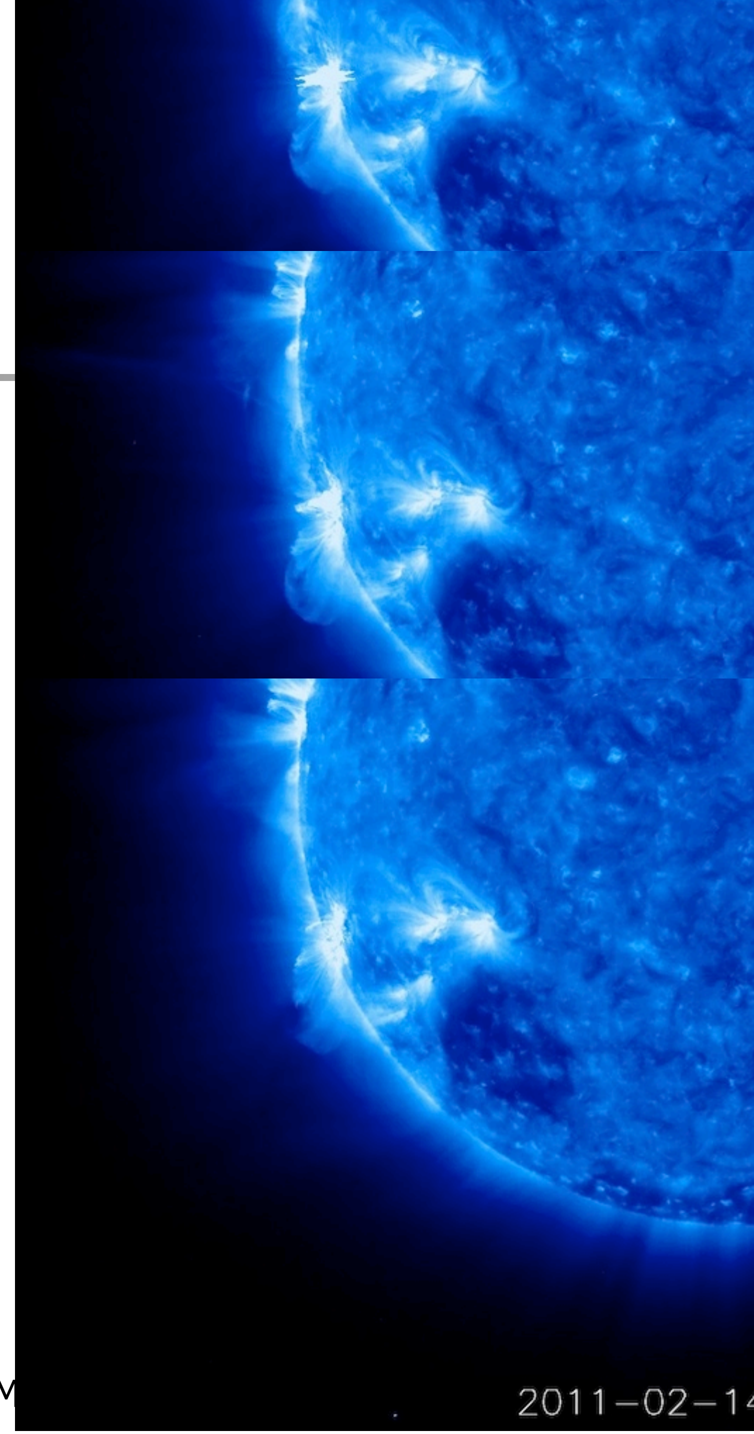

ISSI Coronal M

Some coronal structures are stereoscopically reconstructed

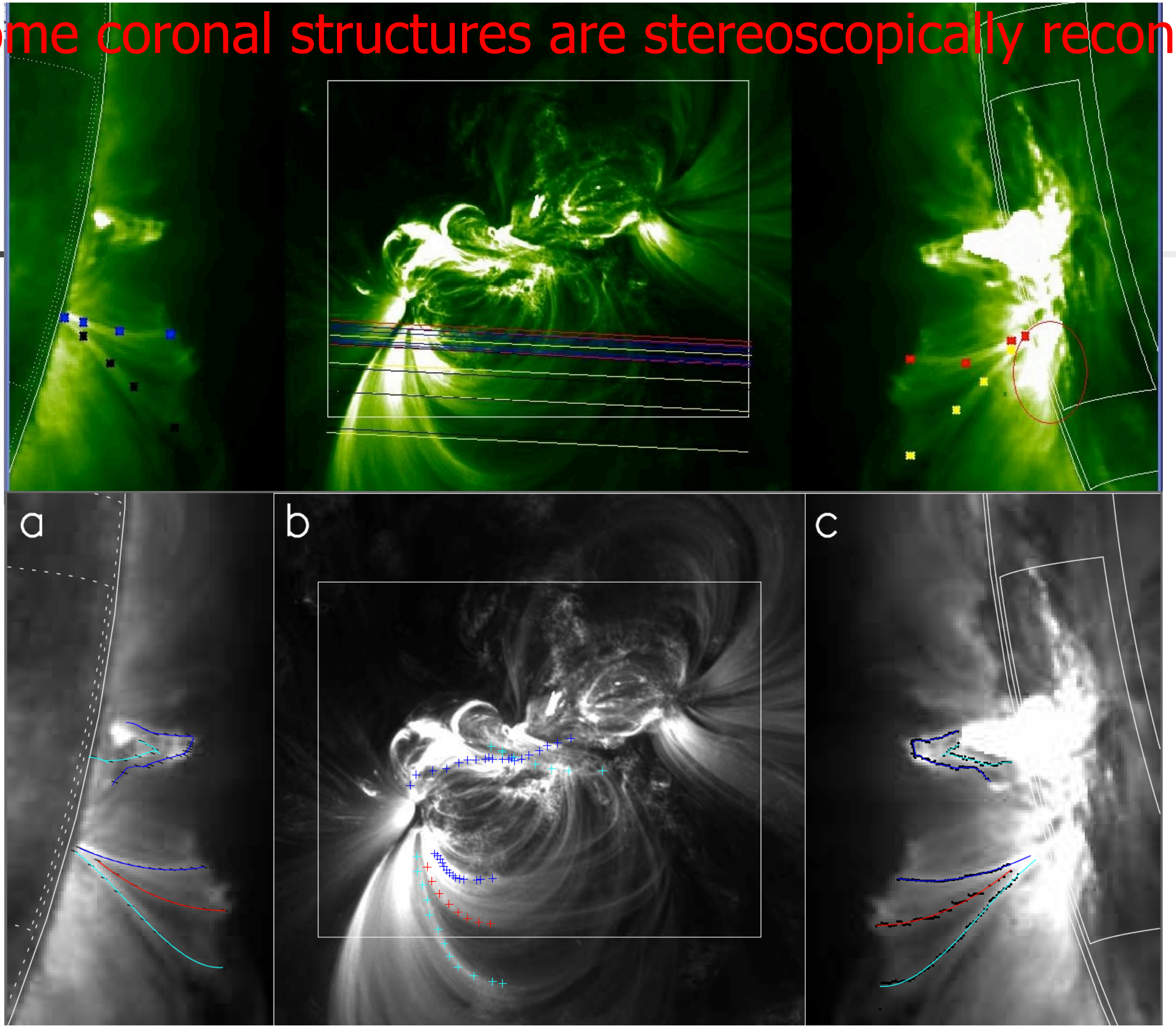

(Dr. W. T. Thompson is acknowledged for correcting STEREO A/B locations)

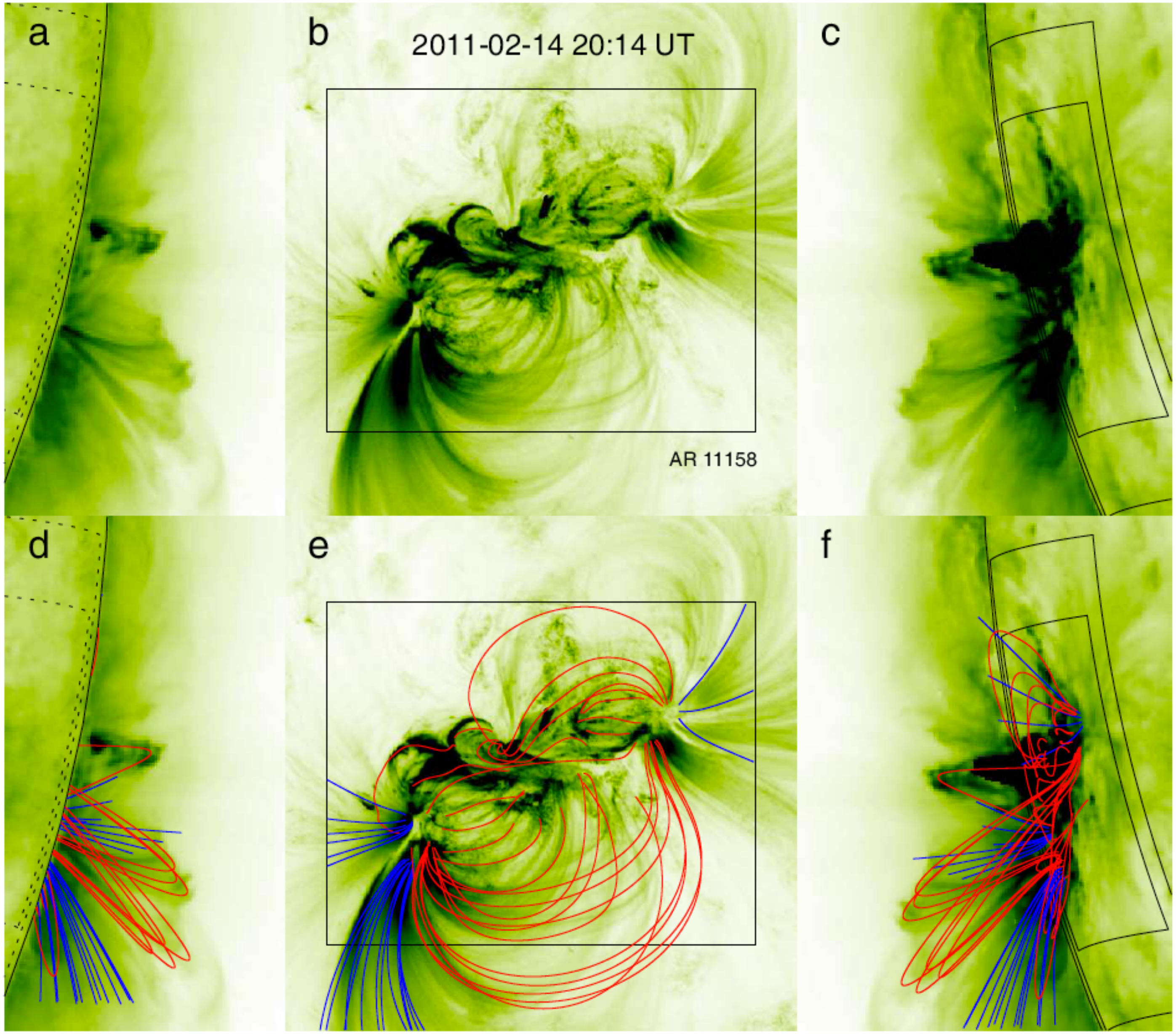

250x200x100 internal grids:

fi = 0.078, or angle <B , J> less than 4.5deg

gi = 0.00067

➔Numerically approximate force-free

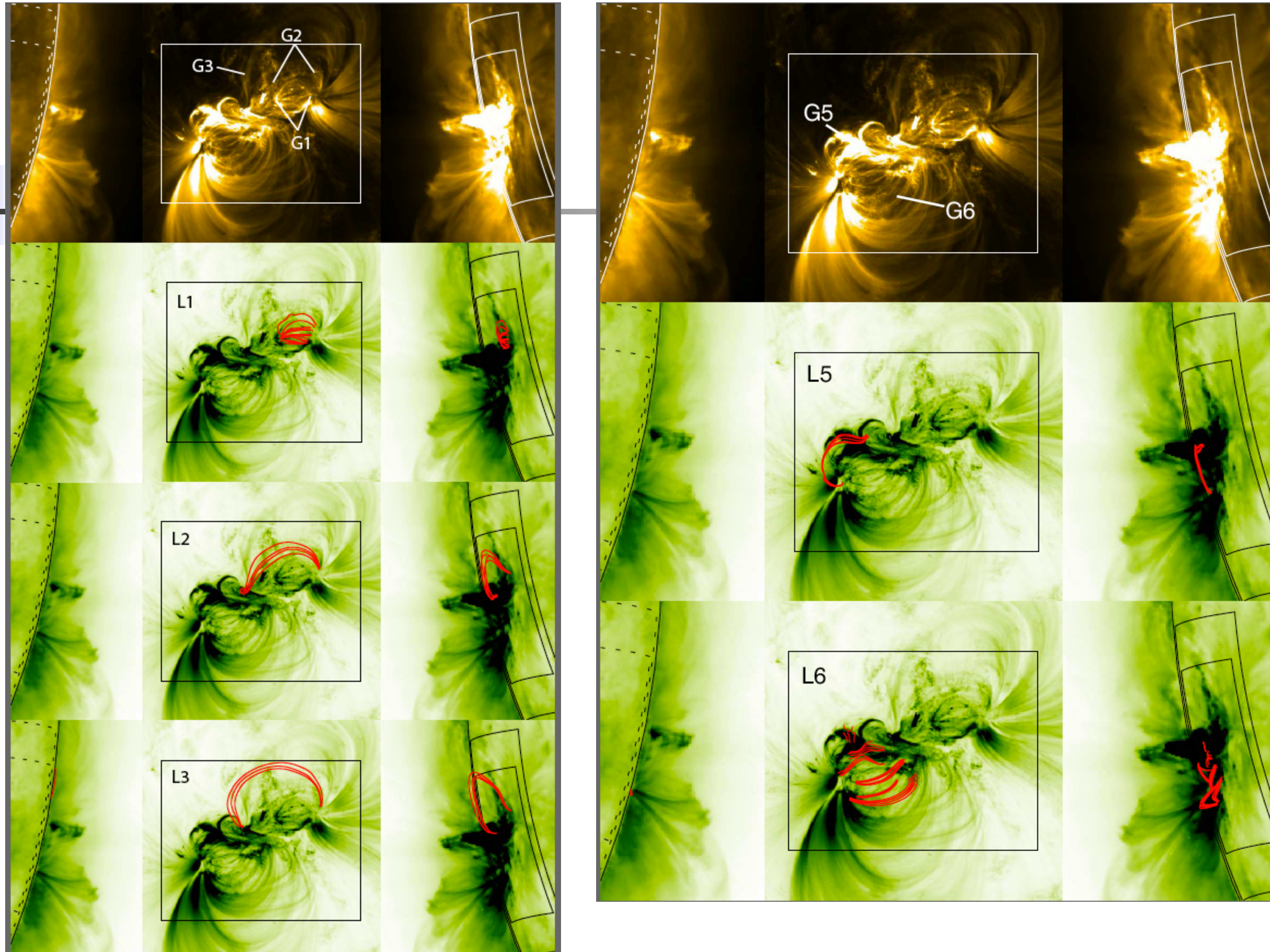
G2
G3
G1
L1
L2
L3
G5
G6
L5
L6

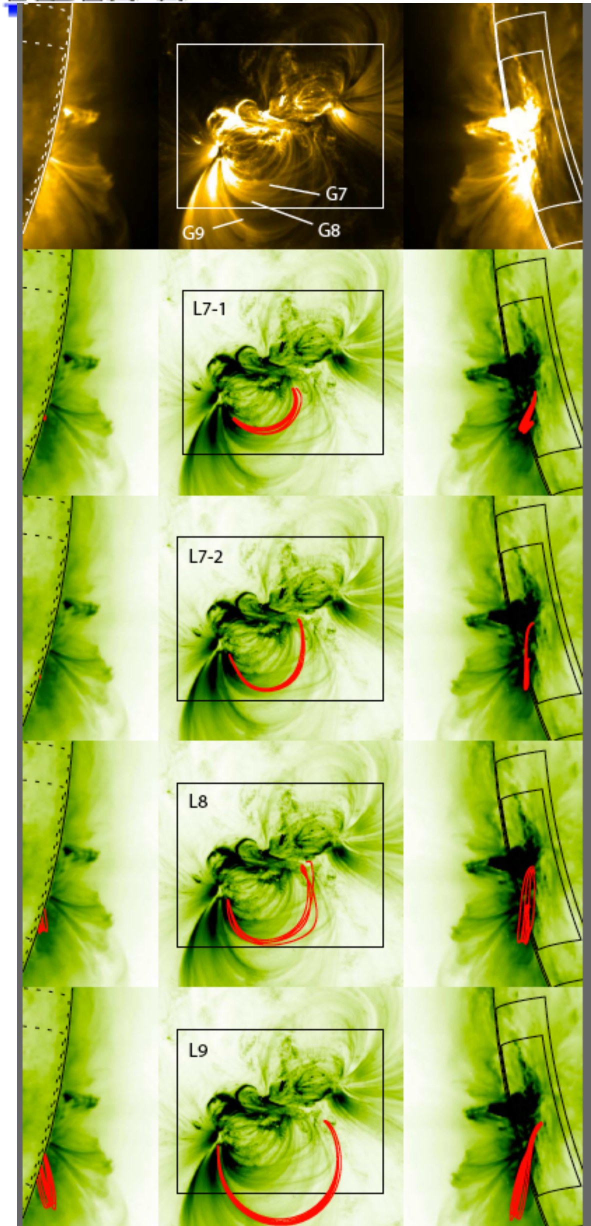

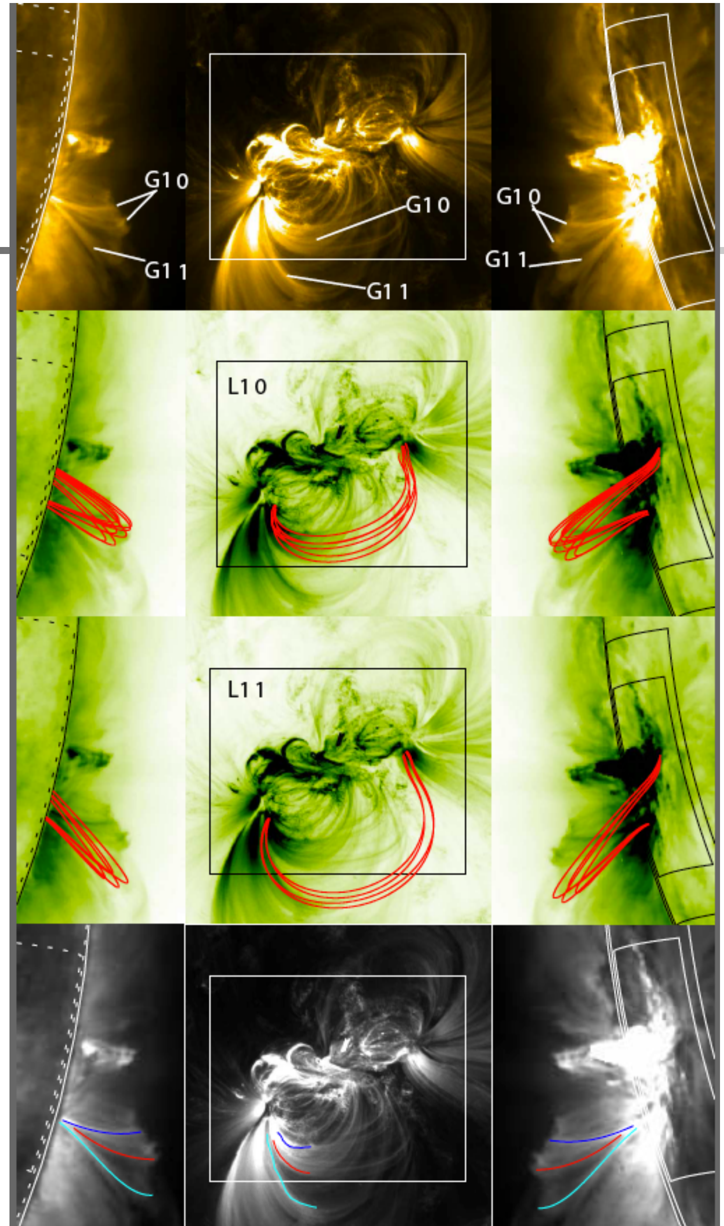

Without stereoscopic information, only LOS co-alignments may not provide correct coronal configuration.

- Misalignment angles of 16-18 deg
- better than other NLFFF models (24 – 44) (DeRosa et al. 2009)
- same order as a model (11-22) with reconstructed loops as constraints (Sandman & Aschwanden 2011)

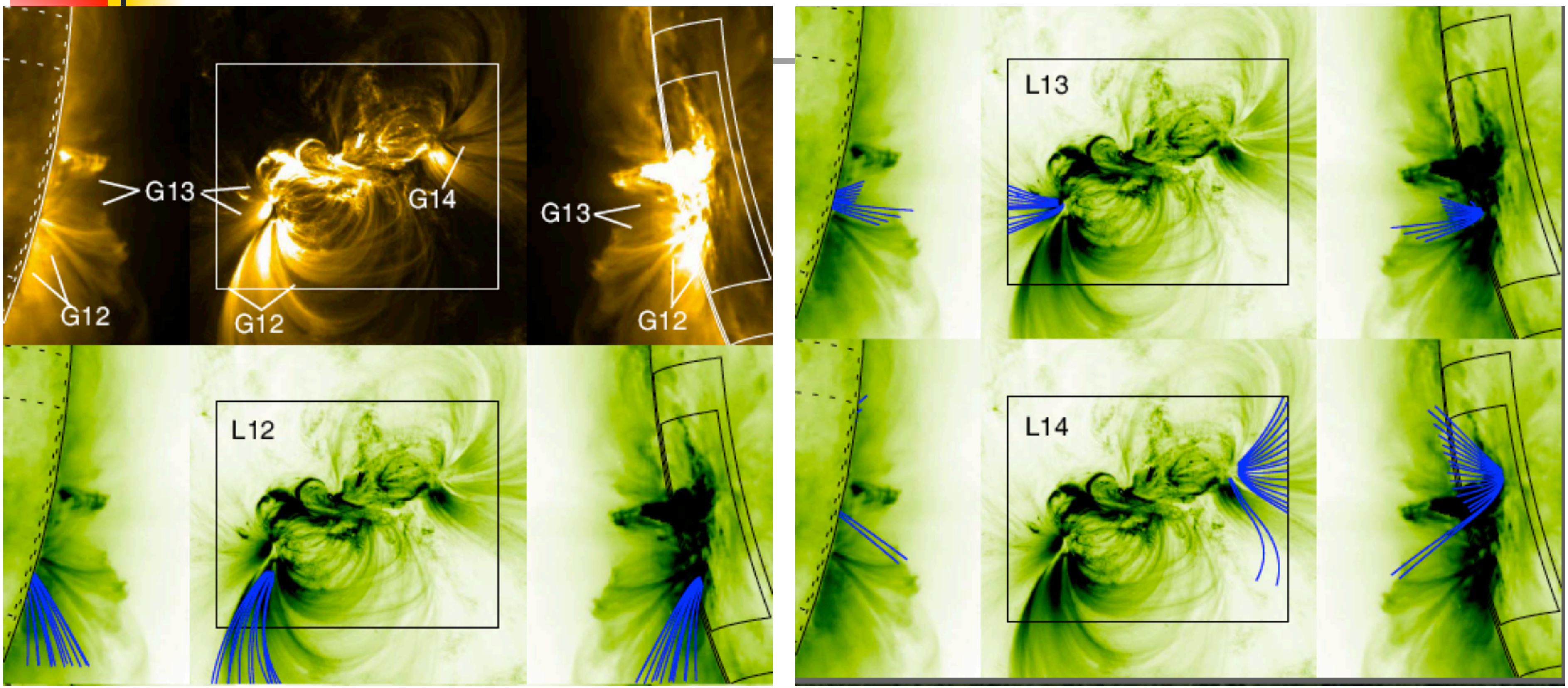
G13
G14
G13
G12
G12
G12
L12
L13
L14

The highly-twisted lower-lying field lines agree with the filament channel

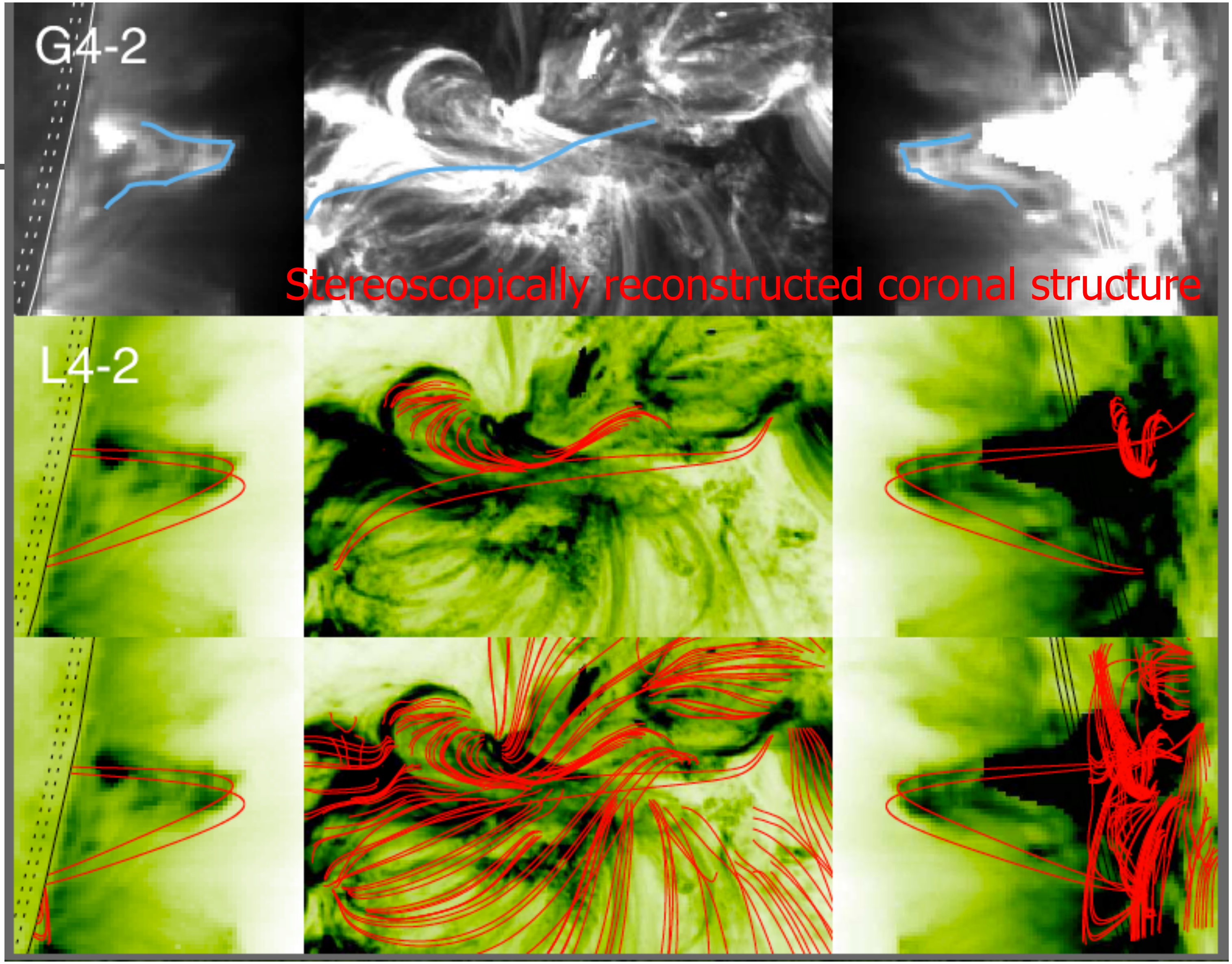

The highly-twisted lower-lying field lines agree with the filament channel

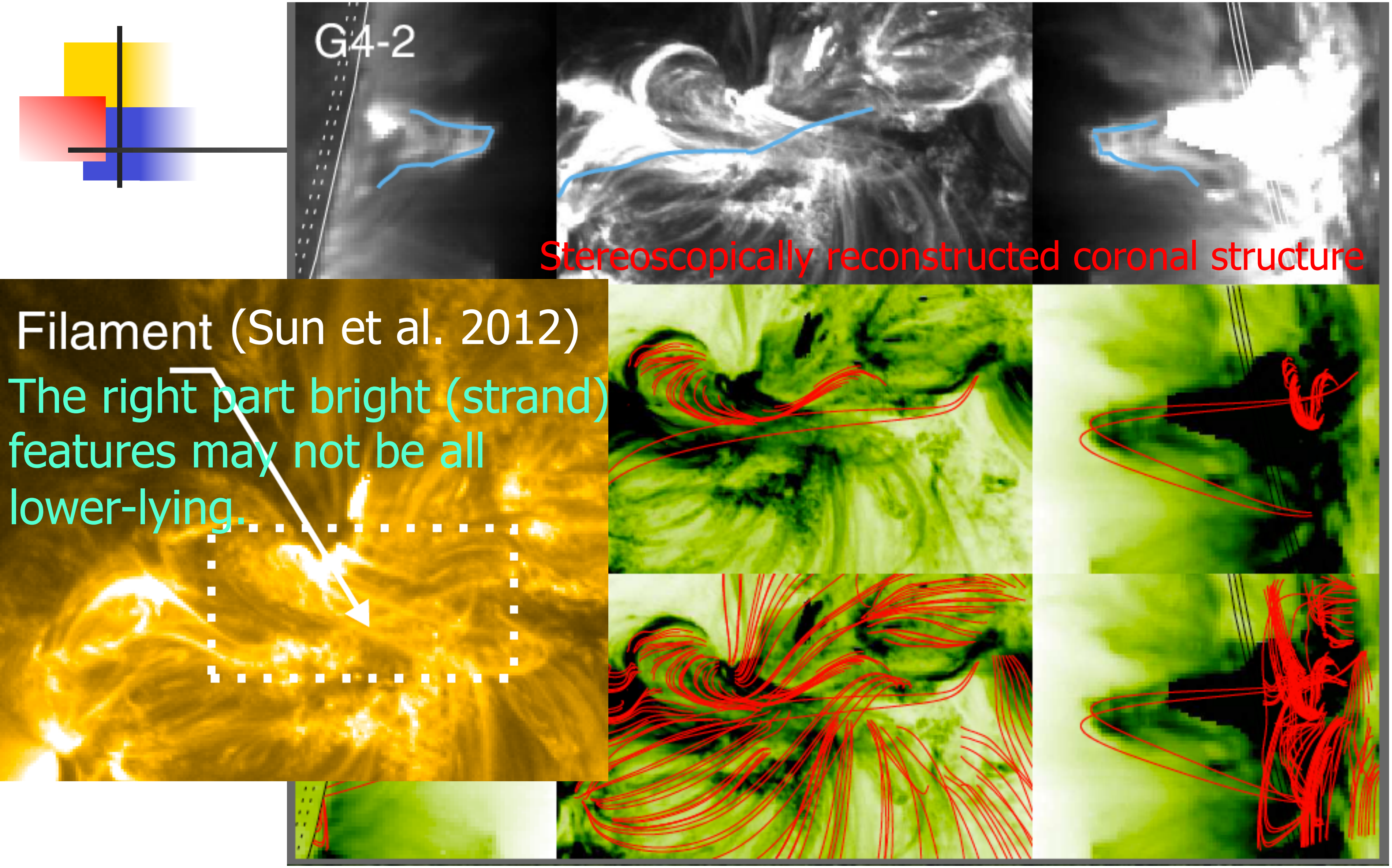

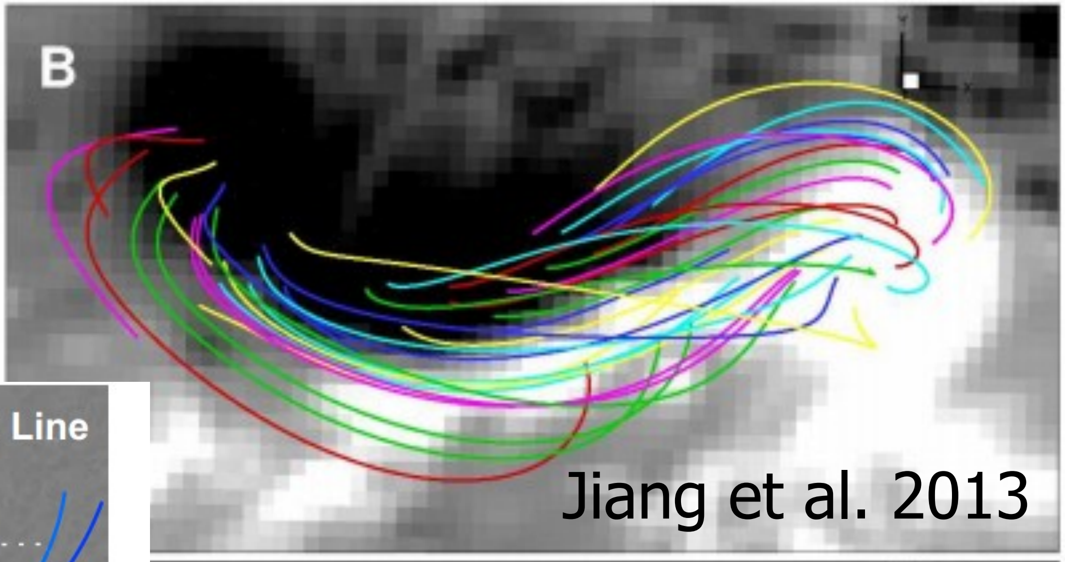
B
Jiang et al. 2013

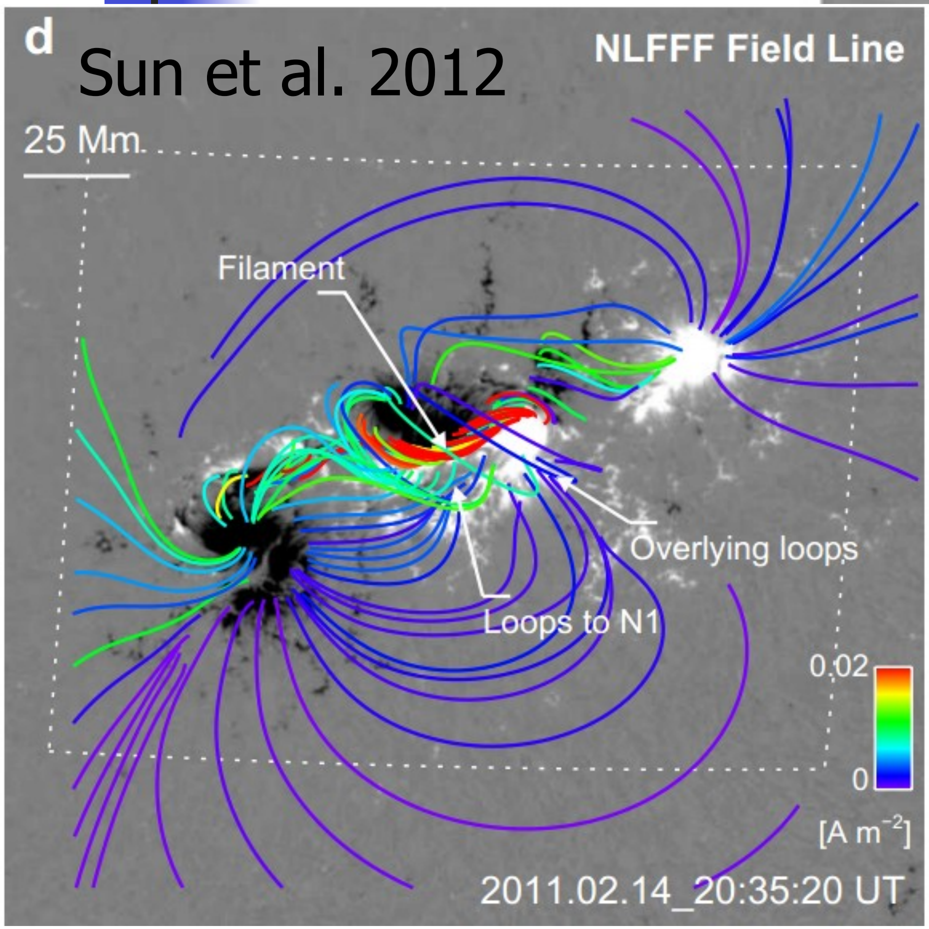
d
Sun et al. 2012
NLFFF Field Line
25 Mm
Filament
Overlying loops
Loops to N1
0.02
0
[A m⁻²]
2011.02.14_20:35:20 UT

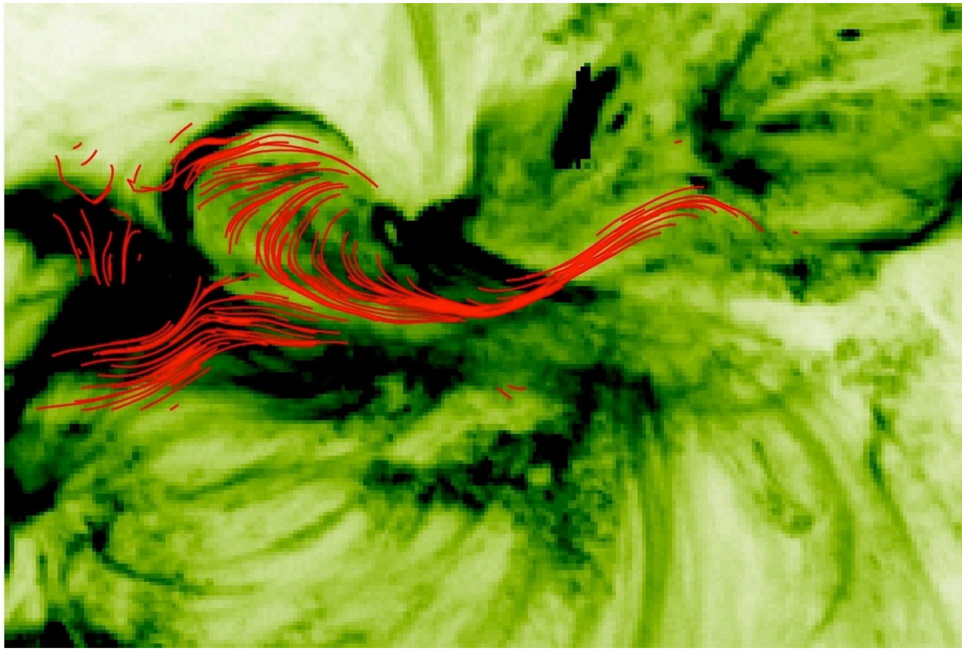

The filament channel in a pivot location

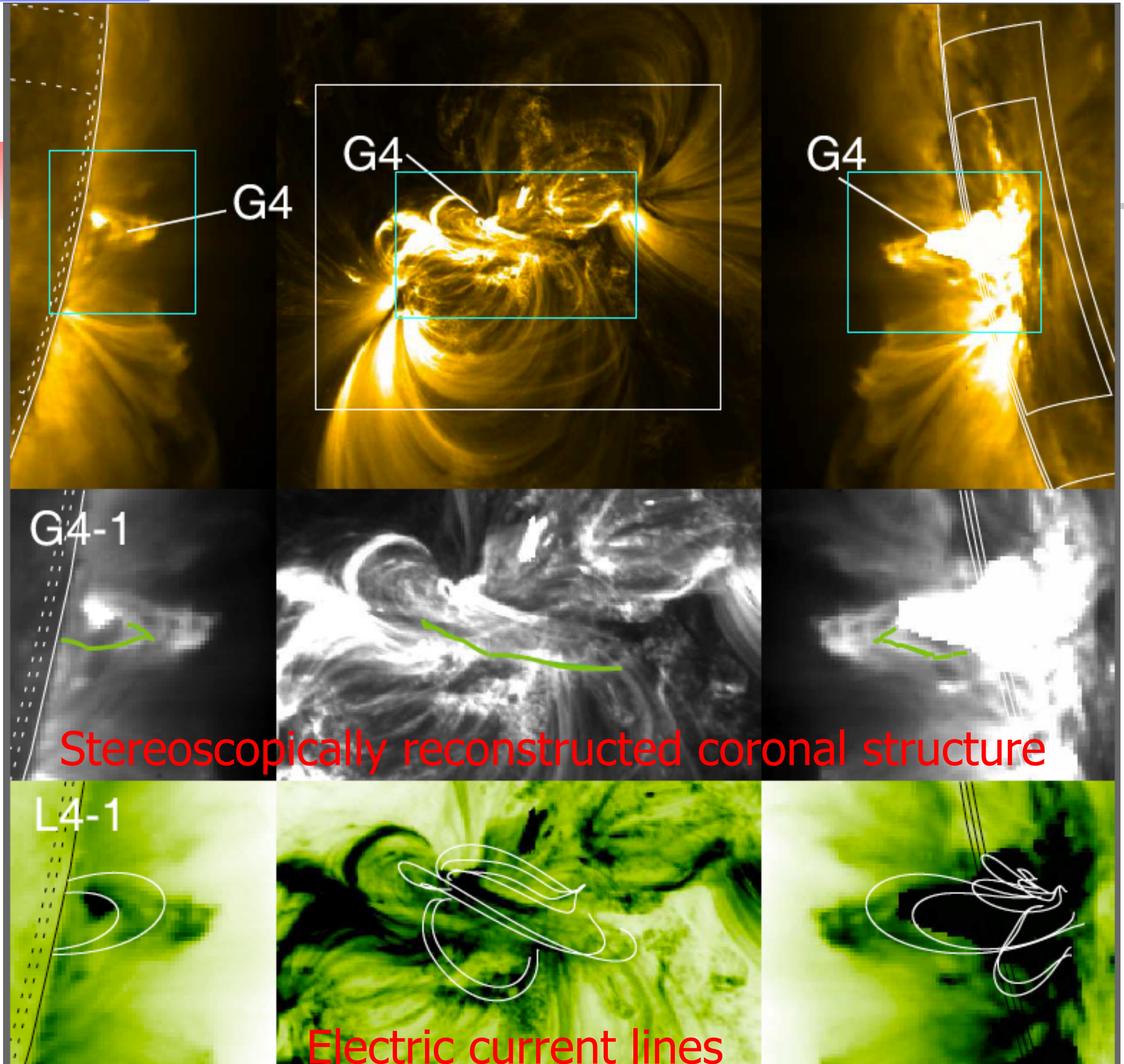

- Obtained current lines but no low-lying field lines across filament
- Misalignment angle between B and the current line is 13.6 deg
- Probably due to inconsistency with force-freeness and errors in PIL region

Pt.1 Summary

(Ref. Wang, Yan & Tan, Solar Physics, 2013)

- DBIE method is rigorous and practical
- Reconstructed fields in AR 11158 stereoscopically agree with SDO, STEREO A/B loops in 3-D.
- Enlongated lower-lying twisting field lines co-spatial with S-shaped filament channel along PIL may be associated with X2.2 flare. However, one cannot simply attribute all EUV bright (strand) features along PIL to manifestation of filament there without stereoscopic information.
- Co-alignment with LOS images alone may not provide correct coronal configuration. We obtain quantitative misalignment angles of 16-18 deg, better than other NLFFF models (24 – 44), & in the same order (11-22) as with reconstructed loops as constraints.
- Further computational acceleration may be achieved to obtain data-driven reconstructed topological configuration evolution.

Tracking Back Solar Wind to its Photospheric Footpoints (Huang, Yan, Li et al. 2014 SP, in press)

- Motivation: there are two populations of current sheets in the solar wind, and one with large deflection angles may be related to flux-tube boundaries (Bruno et al. 2004; Miao et al. 2011) .
- Examination by:
  - WIND Solar wind data traced back to source-surface
  - PFSS model and daily synoptic charts used to obtain photospheric footpoints
  - Obtain distributions of a series of the jumping times between these footpoints
  - Compare with in-situ current sheets distributions

Procedure: 1AU – 2.5Rs

- Select quasi-stationary period of the solar wind from 2004 to 2005 (CR2012 – CR2037) obtained by ACE and Wind spacecraft (at location Px)
- 1-hour average of in-situ observation data
- solar wind radial velocity Vx assumed constant during the propagation
- propagation time: $$\Delta t = \frac{P_x - 2.5R_s}{V_x}$$
- offset to the longitude: $$D = \frac{360°}{27.2753 \times 86400} \Delta t$$

Solar wind positions at source-surface (2.5Rs, Rs solar radius) are thus obtained.

Source-surface to photosphere

- PFSS model
- Synoptic chart as boundary condition modified by inserting daily map

Note: for each Carrington rotation, 0° and 360° are actually the same location but from data 27 days apart. ➔cause extrapolation incorrect there around !

Carrington rotation map

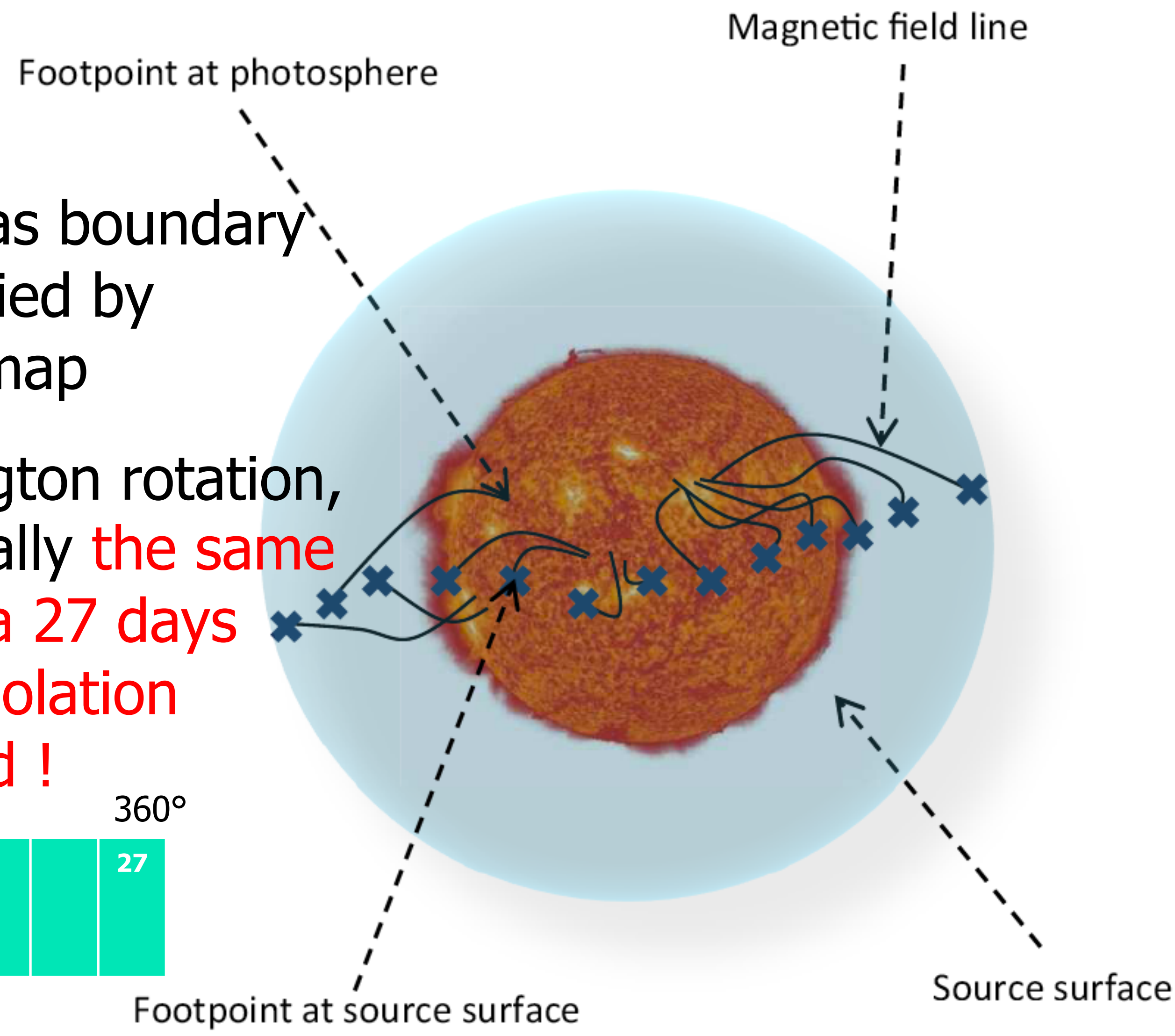

Extrapolation

Inserting daily synoptic chart to CR map as boundary data of PFSS, so as to obtain stable daily footpoints, within 1-sigma error during each CR.

It would be ideal to employ running synoptic map as boundary data and make the computation fast.

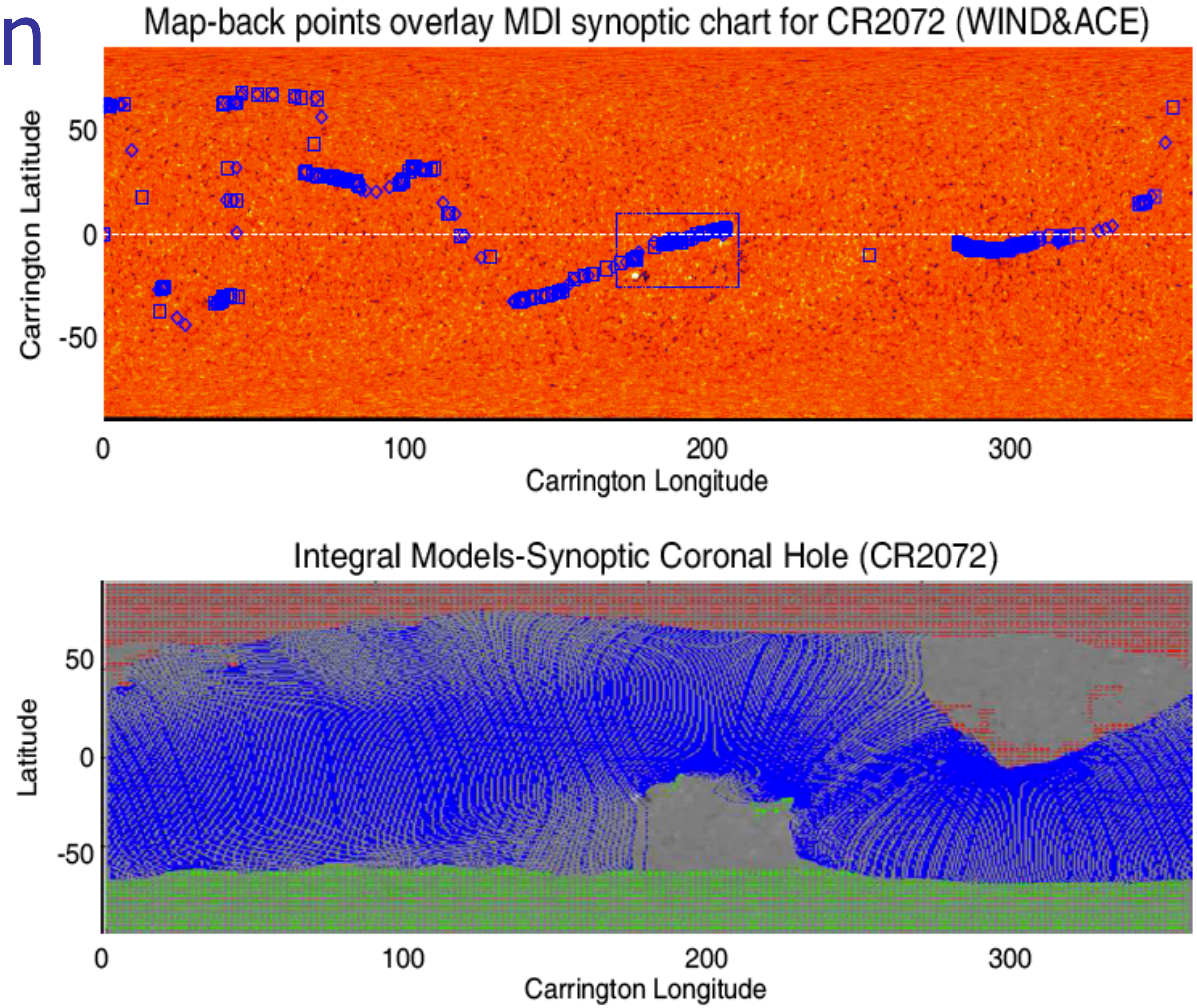

Figure 3. Upper panel: Synoptic chart from SOHO/MDI during CR 2072. The diamonds and squares show the footpoints that trace back from the positions of source surface with *Wind* and ACE data, respectively; the white dashed line represents solar Equator. The detail of the blue frame region will be shown in Figure 4. Lower panel: The Integral Models Synoptic Coronal Hole from NSO/GONG, the polarities of both the open ecliptic-plane flux and the coronal holes are indicated by the same color code: green for positive polarity and red for negative polarity. The tallest closed-flux trajectories are in blue.

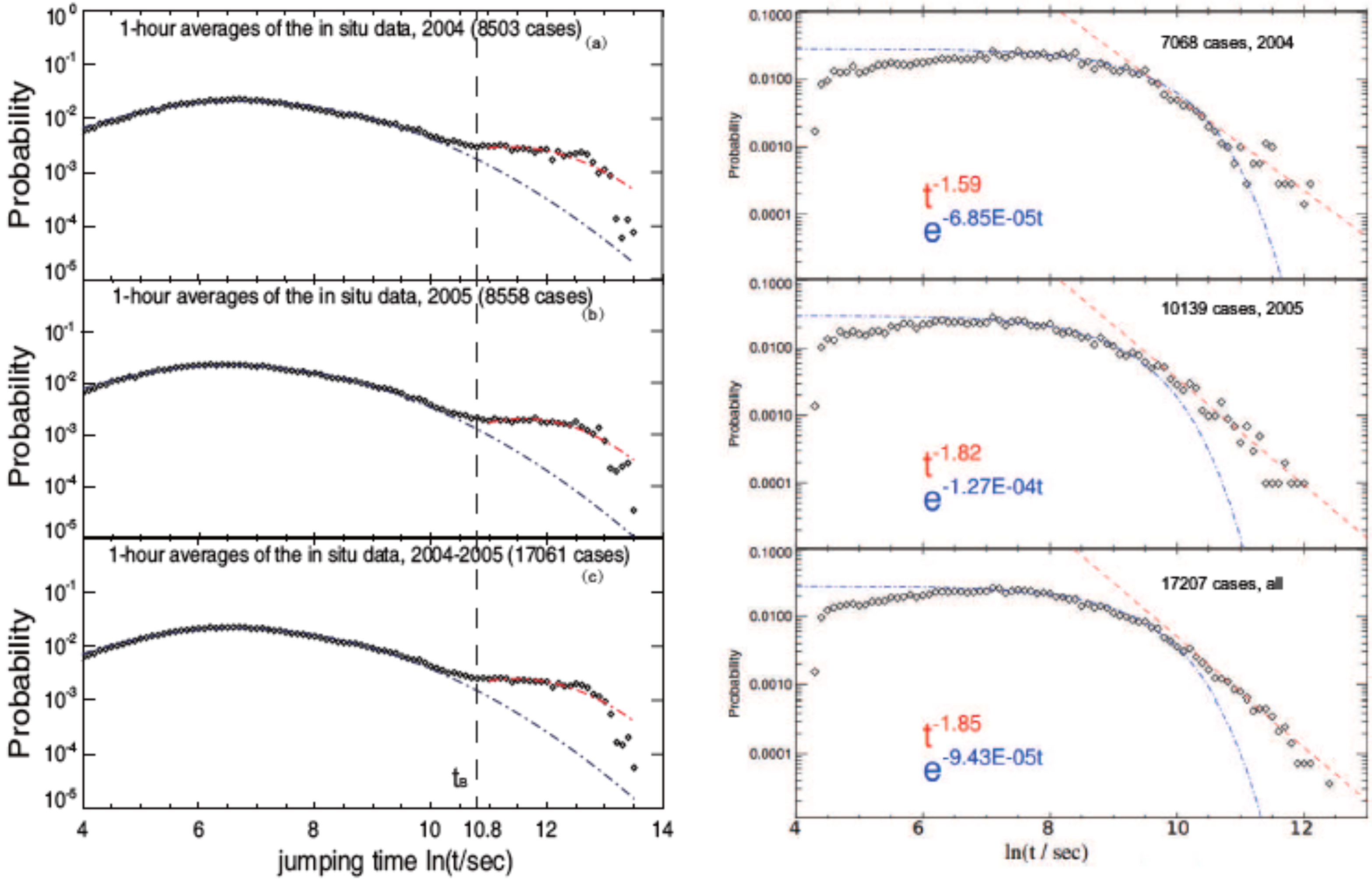

Figure 5. Left panel: Statistical analysis of jump times in different years. Panel a and b are the jump-time analysis in 2004 and 2005, respectively. And panel c is the jump-time analysis for all cases. Right panel: Statistical analysis of waiting times of current sheets with all deflection angle in different years (Miao, Peng, and Li, 2011). From top to bottom, the three panels are the waiting-time analysis in 2004, 2005, and all cases, respectively. The vertical dashed line is the time at break point, t_B. The y-axis is the logarithm of the probability density and the x-axis is the logarithm of the jump time, [ln(t)], where t is expressed in seconds.

Cross boundaries of magnetic cells

- Jump-time statistics of footpoints that cross the boundaries of magnetic cells have similar distribution.
- Supports the scenario that CSs may originate from same mechanism.
- Derivation at small scale regime may be due to that footpoints are more clustered near cell boundaries, leading to more small-scale jump times.

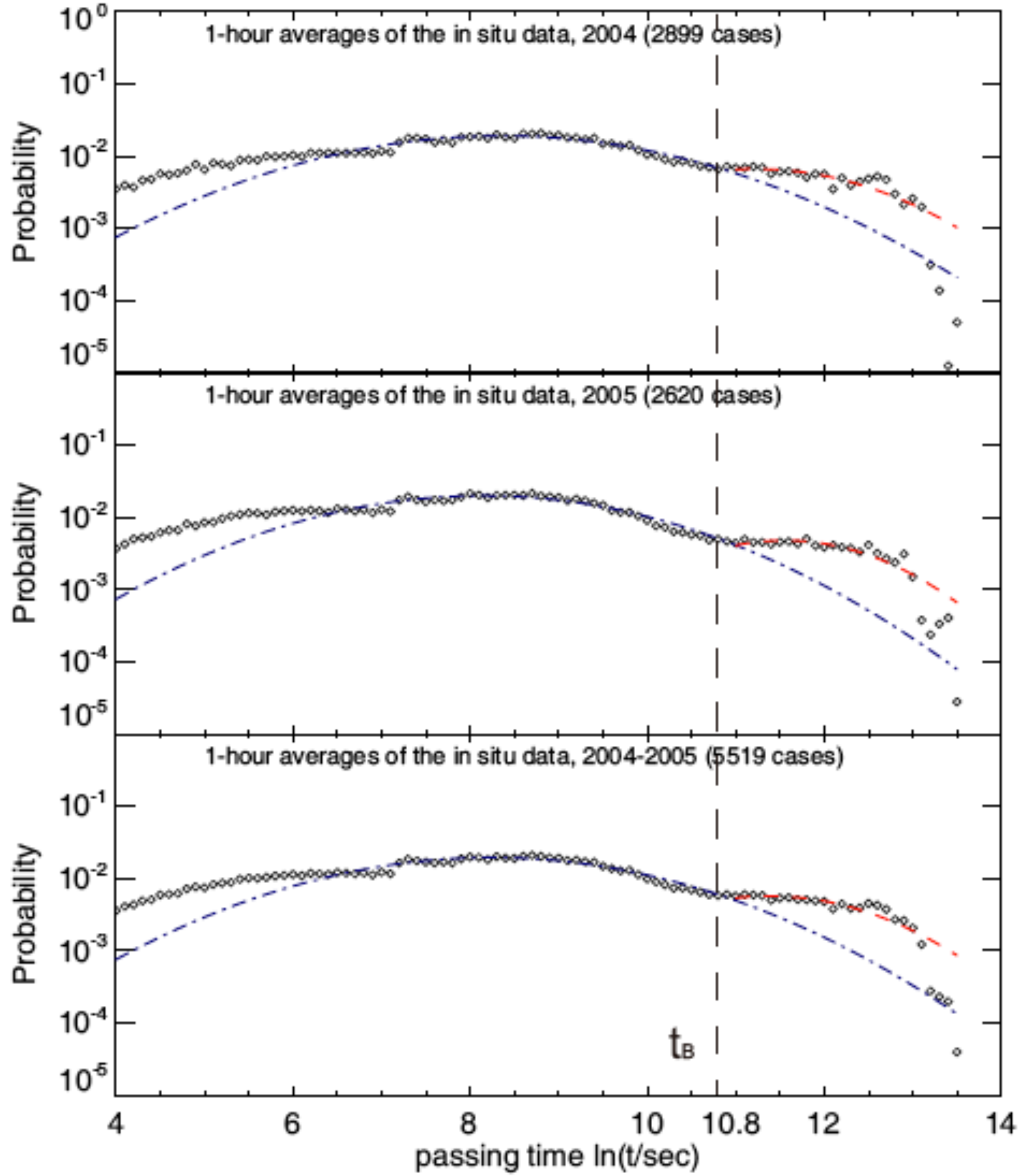

Figure 6. Statistical analysis of the jump times when jump are crossing the boundary of magnetic network in different years. From top to bottom, they are for 2004, 2005, and both years respectively. The y-axis is the logarithm of the probability density and the x-axis is the logarithm of jumping time, [ln(t)], where t is expressed in seconds.

Pt-2 Summary
(Huang, Yan, Li et al. SP, 2014)

- Obtain a total of 17061 jumpings between adjacent footpoints for 2004 and 2005. among them, 5519 have boundary crossings.
- Populations of jumping times are with both small and large jump-time scales.
- Average jump time that cross the boundaries of the magnetic network is longer than the average jump time of all footpoints; consistent with Miao et al （2011）results：CS waiting times with all deflection angles are shorter than that of large deflection angle CSs.
- There could be a physical connection between the flux tube at the solar surface and the 1AU large CS observed from the in-situ data.

CSRH Motivations:

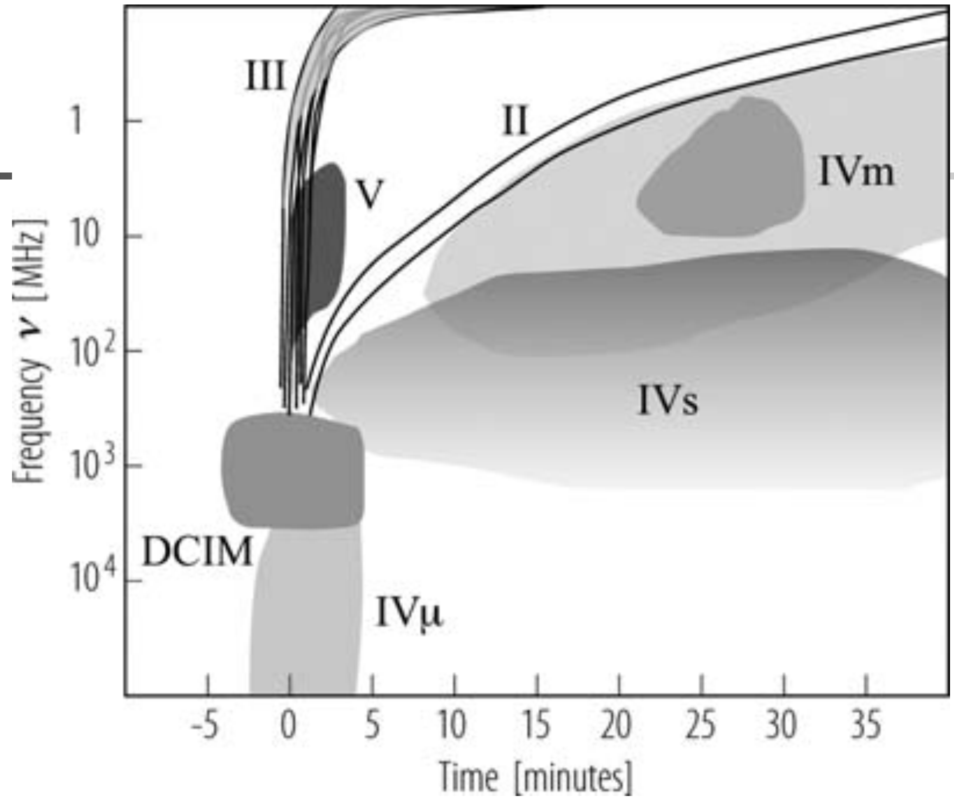

（Benz 2009）

Imaging spectroscopy over cm-λ & dm-λ is important for addressing the problems of primary energy release, particle acceleration, and transportation processes, and the coronal magnetic fields (Bastian, et al., ARAA, 1998; Gary & Keller 2004; Aschwanden 2004; Pick & Vilmer 2008).

40 - 150 MHz Gauribidanur, India

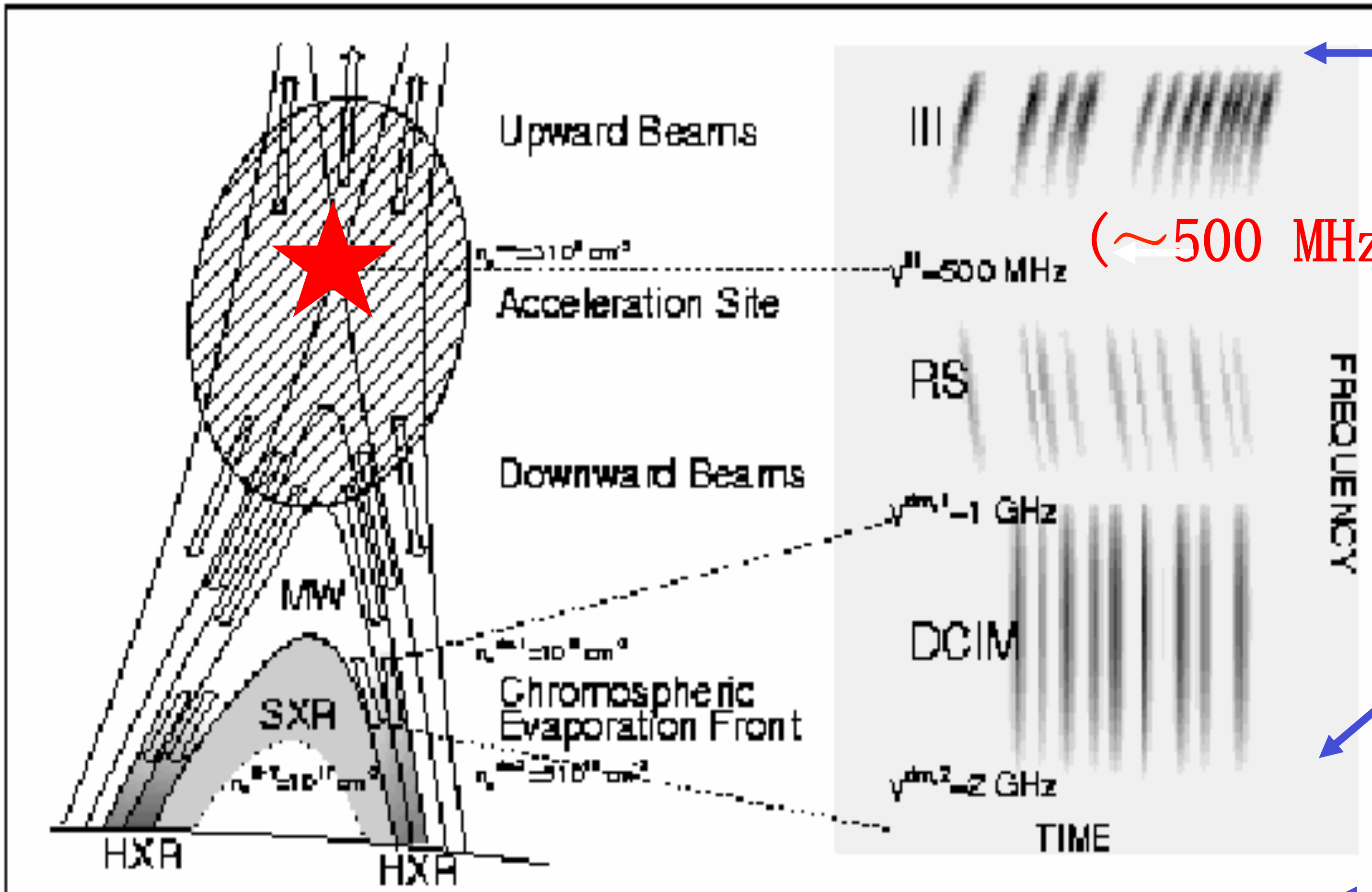

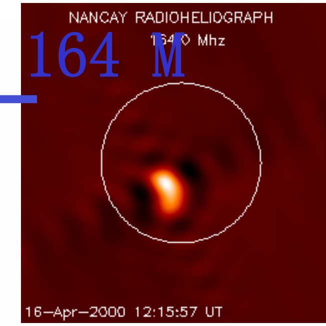

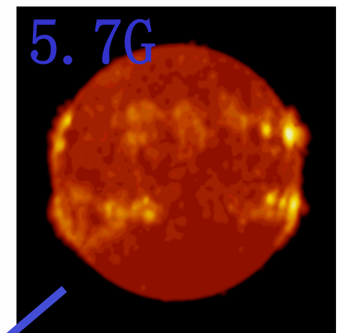

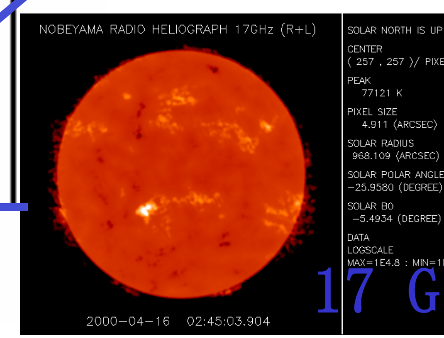

Solar bursts

Aschwanden et al.

Type III bursts in 5-Nov-1998 flare:

12 TROTTET ET AL.

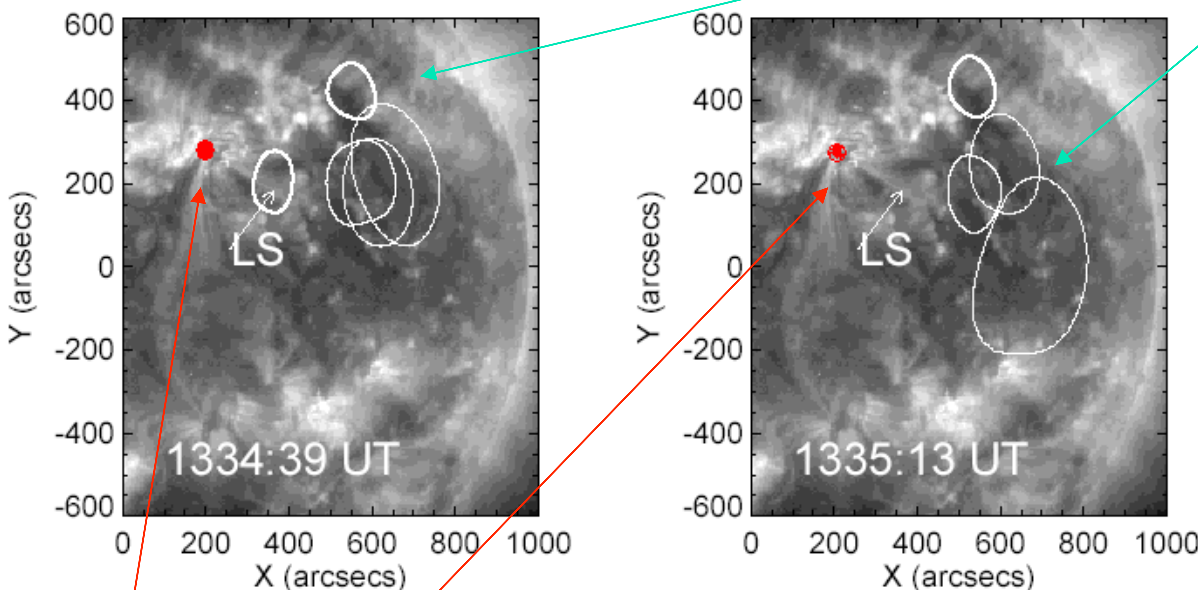

Yohkoh HXRs

Figure 6. Typical pattern of the bursts observed by the NRH at 410, 327, 236 and 164 MHz before 1334:53 UT (left) and after 1334:53 UT (right) overlaid on the 195 Å EIT image taken at 1324:34 UT. For each frequency the contour level correspond to 70% of the maximum brightness of the image (410, 327, 236, 164 MHz in the order of increasing size and decreasing thickness). LS1 refers to a large-scale loop system seen by EIT (see text)

Radio bursts at 410, 327, 236, & 164 M with thinner lines and larger size

Trottet, et al. (2006, Sol. Phys.)

Type III bursts in 5-Nov-1998 flare:

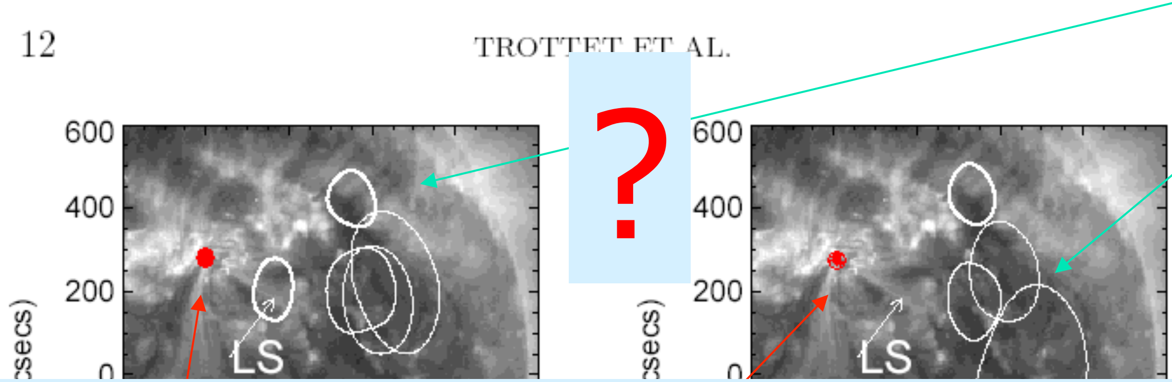

Radio bursts at 410, 327, 236, & 164 M

Why the radio and HXR sources are not aligned but, instead, in perpendicular?

⇒Need multi-wave imaging observations in dm-cm (≥ 400MHz) ranges!

Trottet, et al. (2006, Sol. Phys.)

20-Feb-2002 flare event:

Radio bursts at 410 MHz

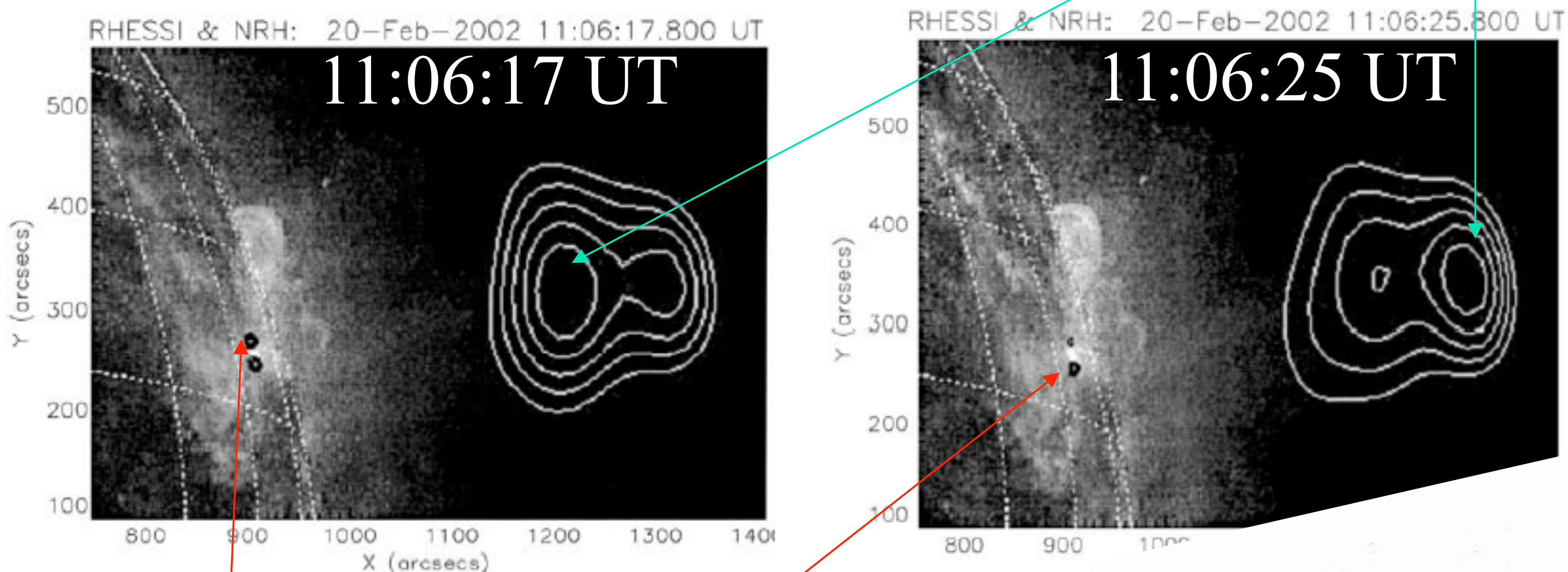

Figure 3. RHESSI iso-contours (*black*) (40, 60, 80% of the maximum) at 25–40 keV and NRH contours at 410 MHz (*white*) (50, 60, 70, 80, 90%) observed at 11:06:17.800 at the time when similar flux is radiated from sources 1 and 3 (see text). The RHESSI and NRH contours are superposed on the closest EIT image ... images are obtained using grids 3 to 9 giving a resolution of

RHESSI HXRs

Figure 4. Same as Figure 3 at 11:06:25.800 at a time where the southernmost source 3 is predominant (see text). The change of the relative brightness of the two radio components has to be noted.

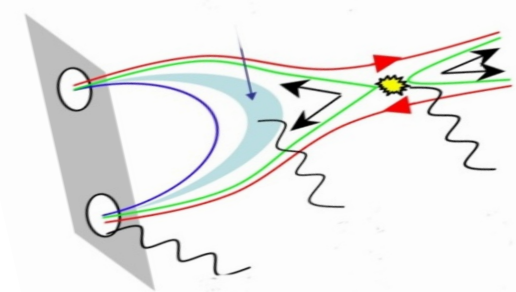

Vilmer, et al. (2002, Sol. Phys.)

20-Feb-2002 flare event:

Radio bursts at 410 MHz

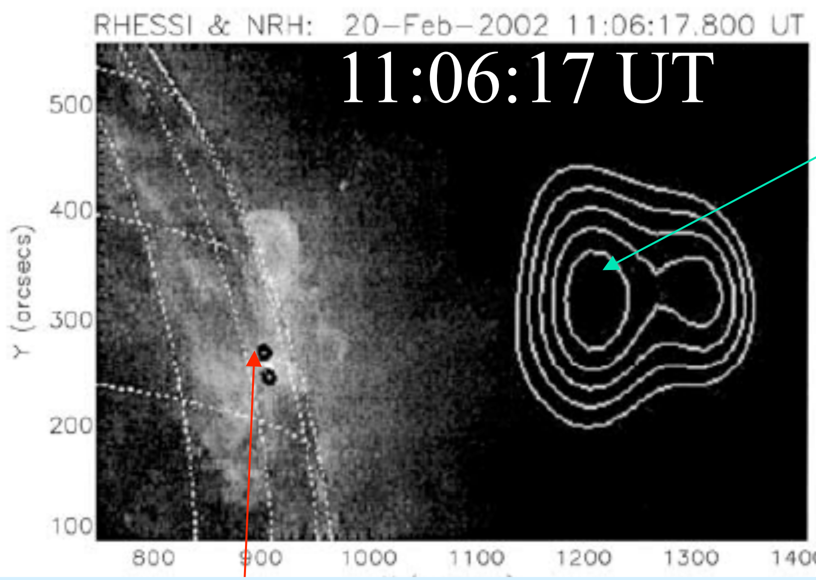

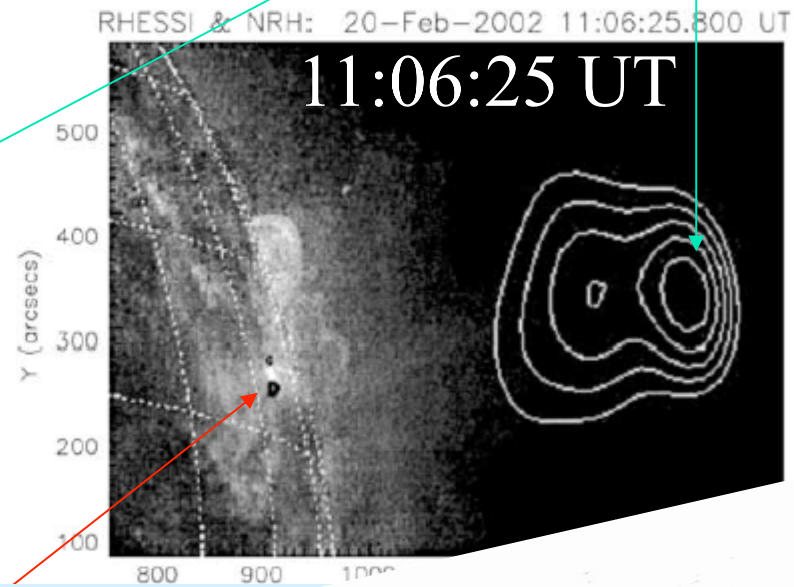

The magnetic structure connecting radio and HXR sources may be due to standard flare model ?

⇒Need multi-wave imaging observations in dm-cm (≥ 400MHz) ranges!

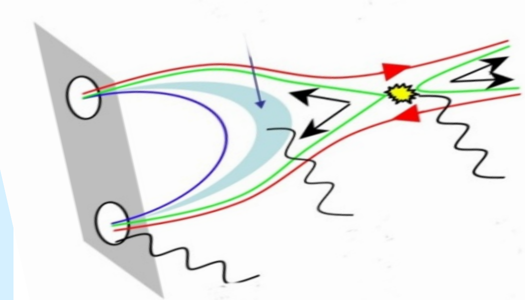

Vilmer, et al. (2002, Sol. Phys.)

Coherent emission: U-burst

30 March 2001

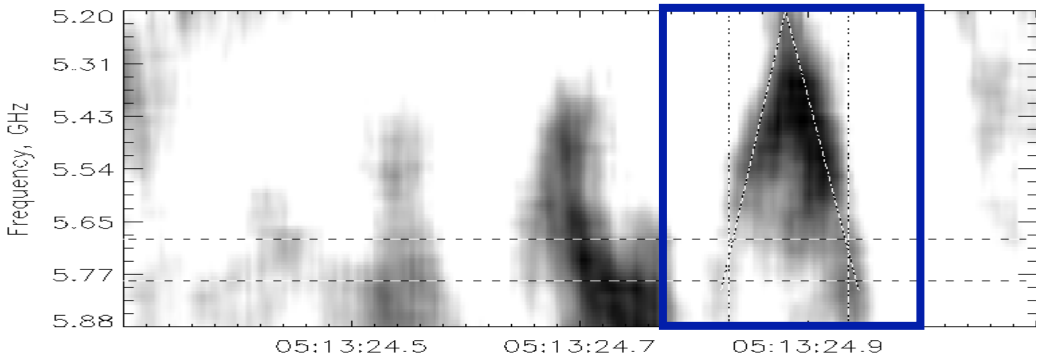

17 September 2001

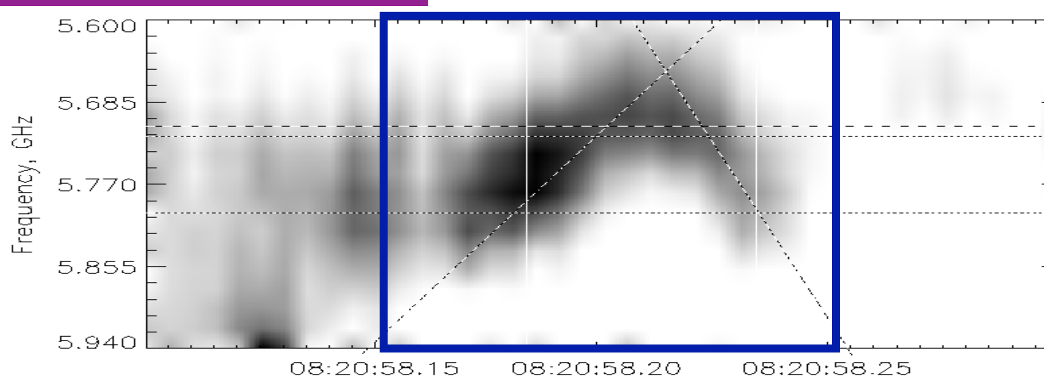

(Altyntsev A.T, et al. 2003, A&A)

- Exciter at meter-decimetric wavelengths: electron beam moving along a magnetic loop with density minimum at the loop top (beam instability, kinematics). Plasma parameters are stationary.
- But the SSRT observations does not show a large distance (>30 Mm) between sources at different branches.
- In cm-wavelengths U-structures are produced by density variations due to a plasma response to a heating pulse. The source size along the loop is order of a few Mm. (Loss-cone instability, MHD time-dependent process)

Bounce period or transverse MHD oscillations of loop?

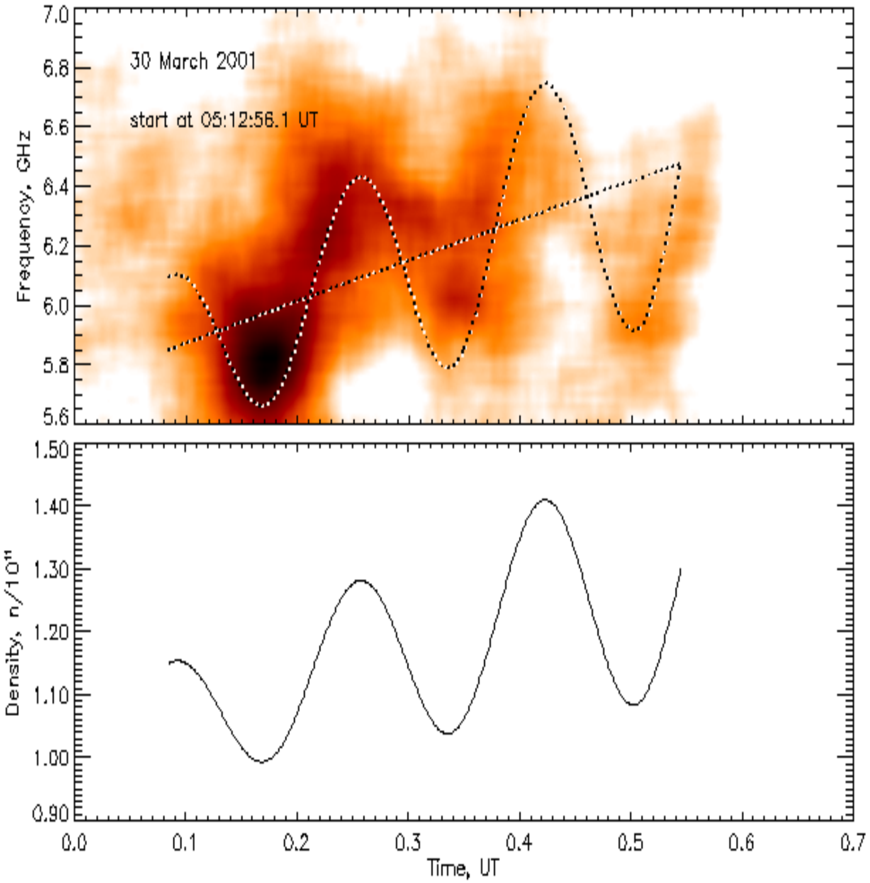

Two variants to explain:

1. Bounce period of the short electron beam in the long magnetic loop.

From lifetime duration follows beam velocity of 0.45c and the loop length about 20 Mm

1. Transverse MHD oscillations of the loop (for B=100 G, diameter of the loop must be about 100 km)

Trend of the frequency drifting rate corresponds to density rising

$$\partial f / \partial t \approx 1.25 \ GHz/s \ \Rightarrow \ \partial n / \partial t \approx 5 \times 10^{10} cm^{-3}/s$$

Altyntsev A.T, et al. (2003, A&A)

“Hinode event” on 13 Dec 2006

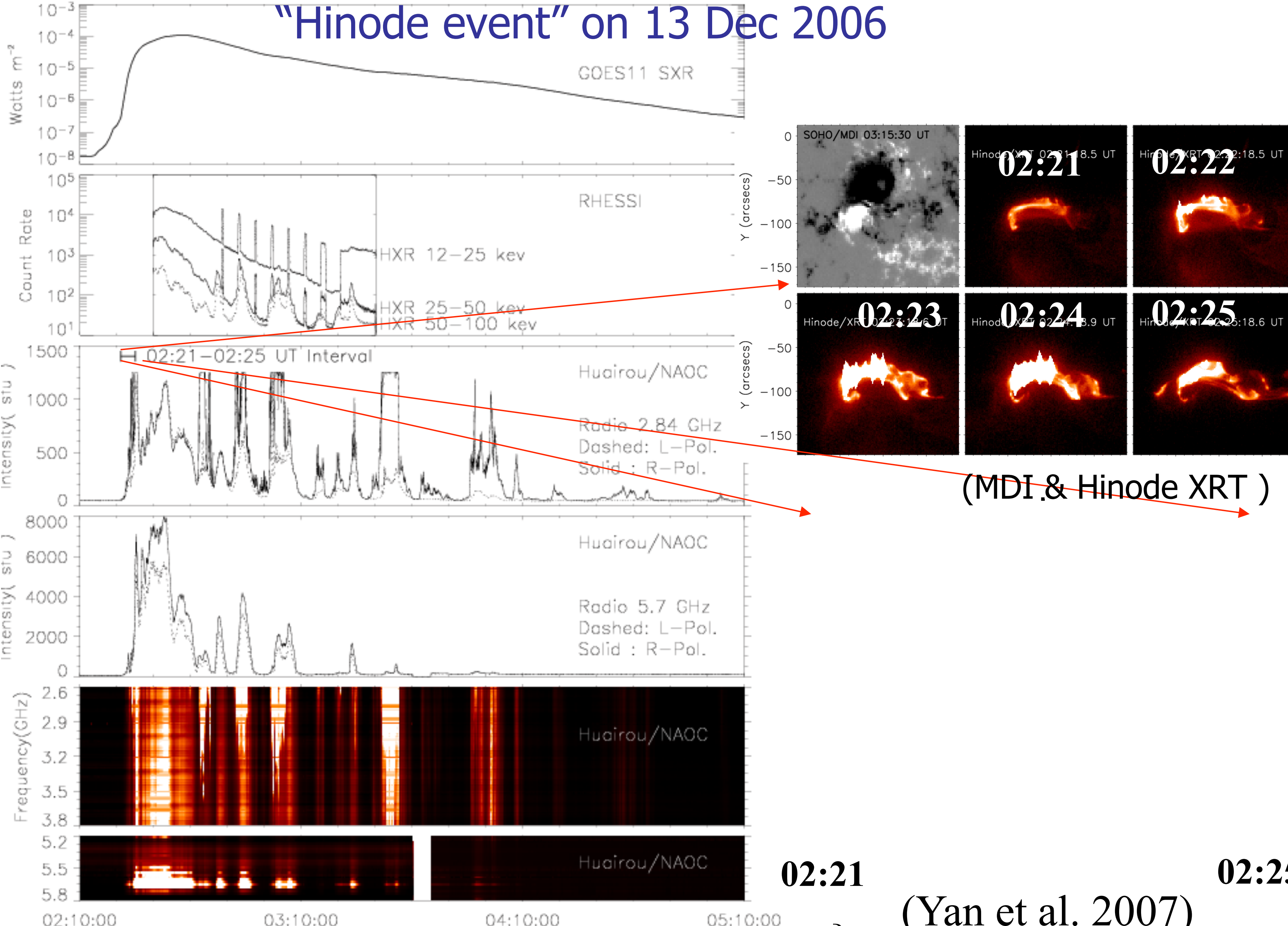

(MDI & Hinode XRT)

02:21

02:25

(Yan et al. 2007)

Statistic study of 74 ZPs show L_n/L_B decreasing (Yu et al. 2013， ApJ)

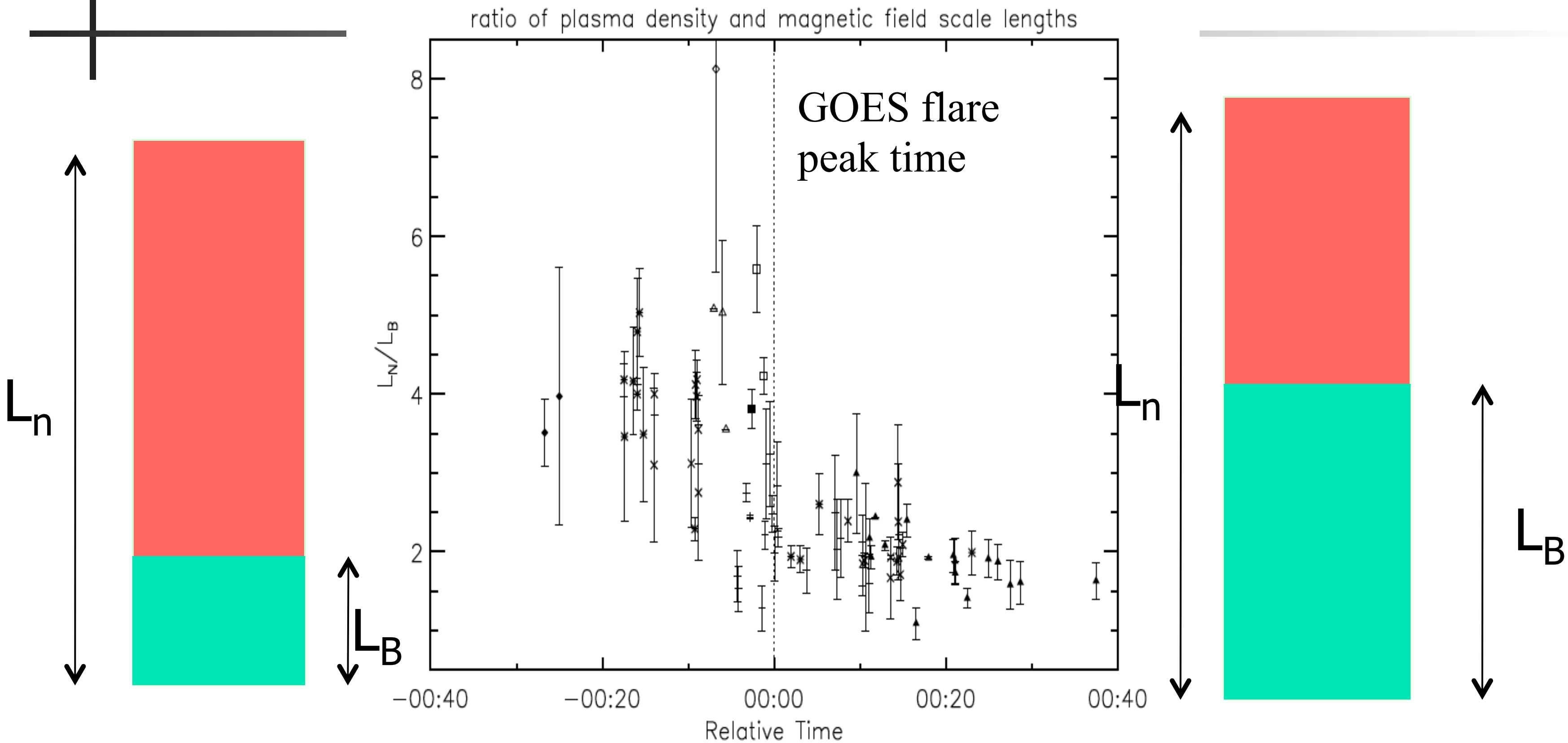

What's the exact magnetic structure?

EVLA Type IIIdm Bursts (Chen et al. 2013 ApJ)

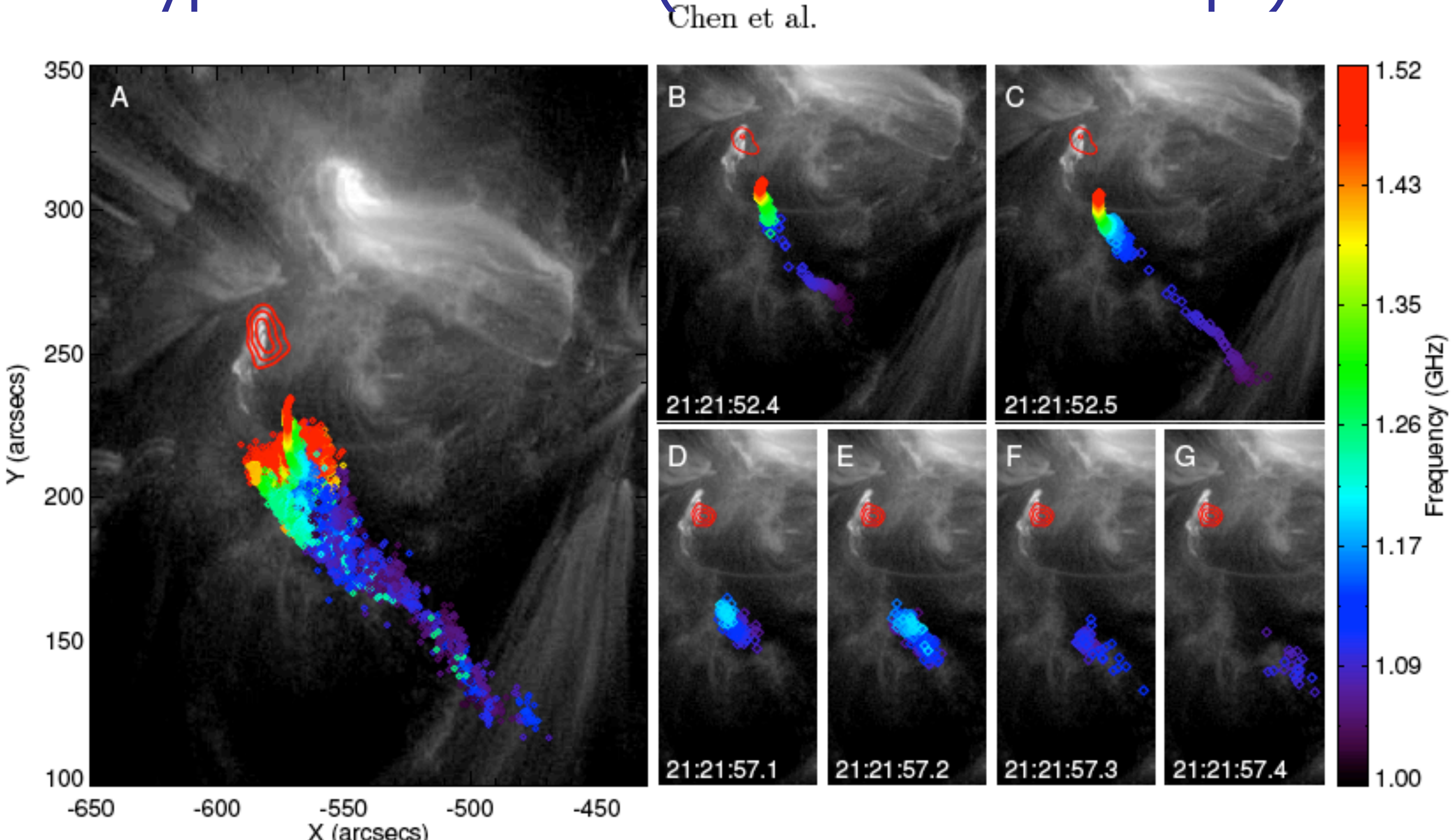

- Along cooler & over-denser coronal "fibrous" loops that are composed of unresolved "strands" and invisible in other band, e.g., EUV images.
- ➔The need of radio imaging spectroscopy!

→ require a new instrument:

capable of true imaging spectroscopy, with high temporal, spatial, and spectral resolution ---- CSRH or FASR(Hudson & Vilmer 2007, Pick & Vilmer 2008, Klein et al 2008).

Technical challenges

- To implement **high cadence imaging** at **wide-band** & **>2 order higher multiple frequencies**
- Data process for such a system

CSRH Specifications

(Yan et al. 2009, Earth, Moon Planet)

Range	~0.4–15 GHz （λ： ~75 –2 cm）	
Frequency Res.	64 chan	(I: 0.4-2 GHz)
	>32(~500) chan	(II: 2-15 GHz)
Spatial Res.	1.3″– 50″	
Temporal Res.	I: ~ 25 ms	
	II: ~200 ms	
Dynamic Range	25 db （snapshot）	
Polarizations	Dual circular L, R	
Array	I: 40×4.5m	
	II: 60×2m parabolic antennas	
Lmax	3 km	
Field of view	0.6°– 7°	

CSRH-I Block Diagram in 400MHz-2 GHz

- **Antennas & feeds**
- **Op T/R & Analog**
- **Digital Correlation**
- **Monitoring**
- **Data Storage & Pre-processing**
- **Image Processing**

Similar for CSRH-II in 2-15 GHz

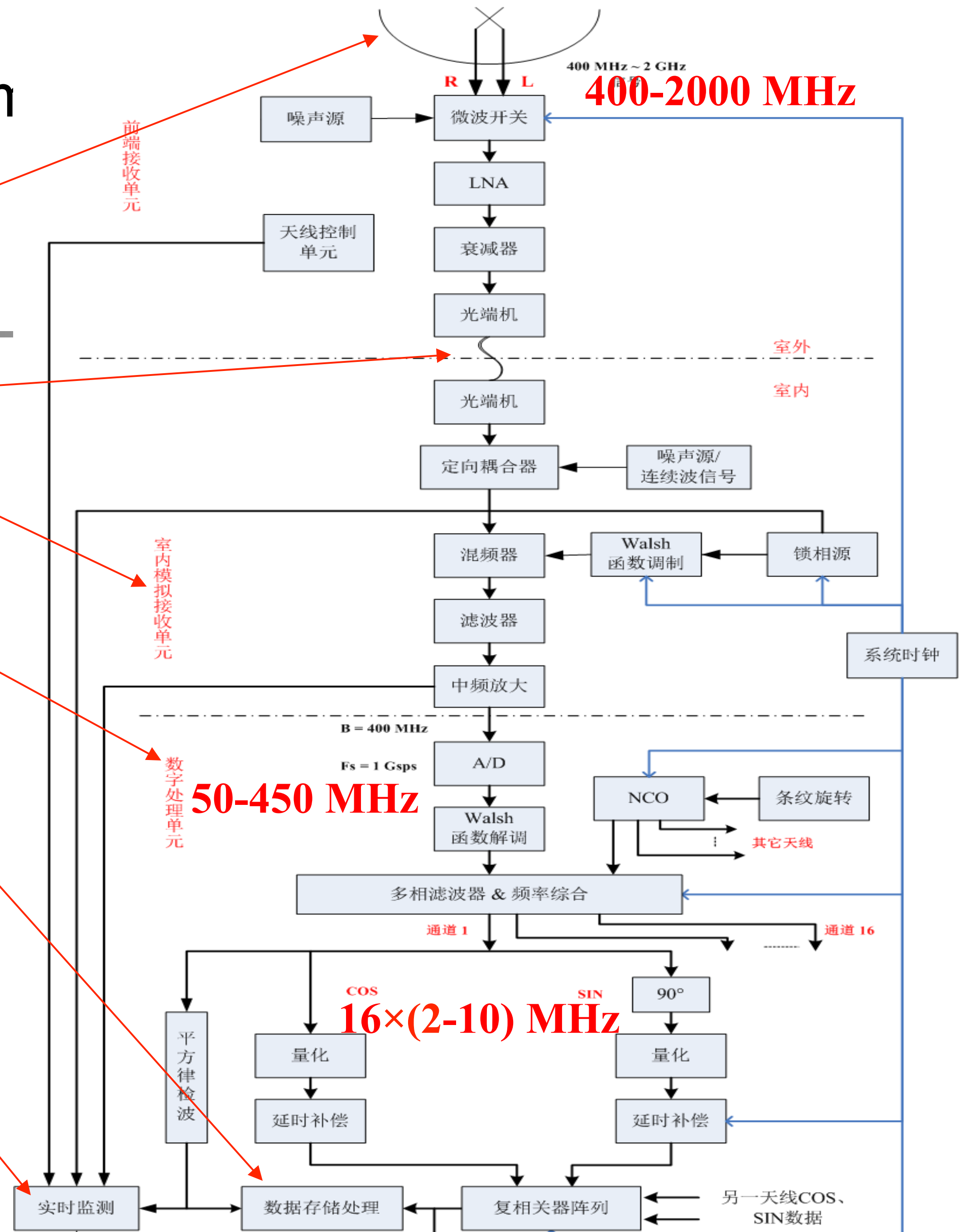

Site and Construction of CSRH

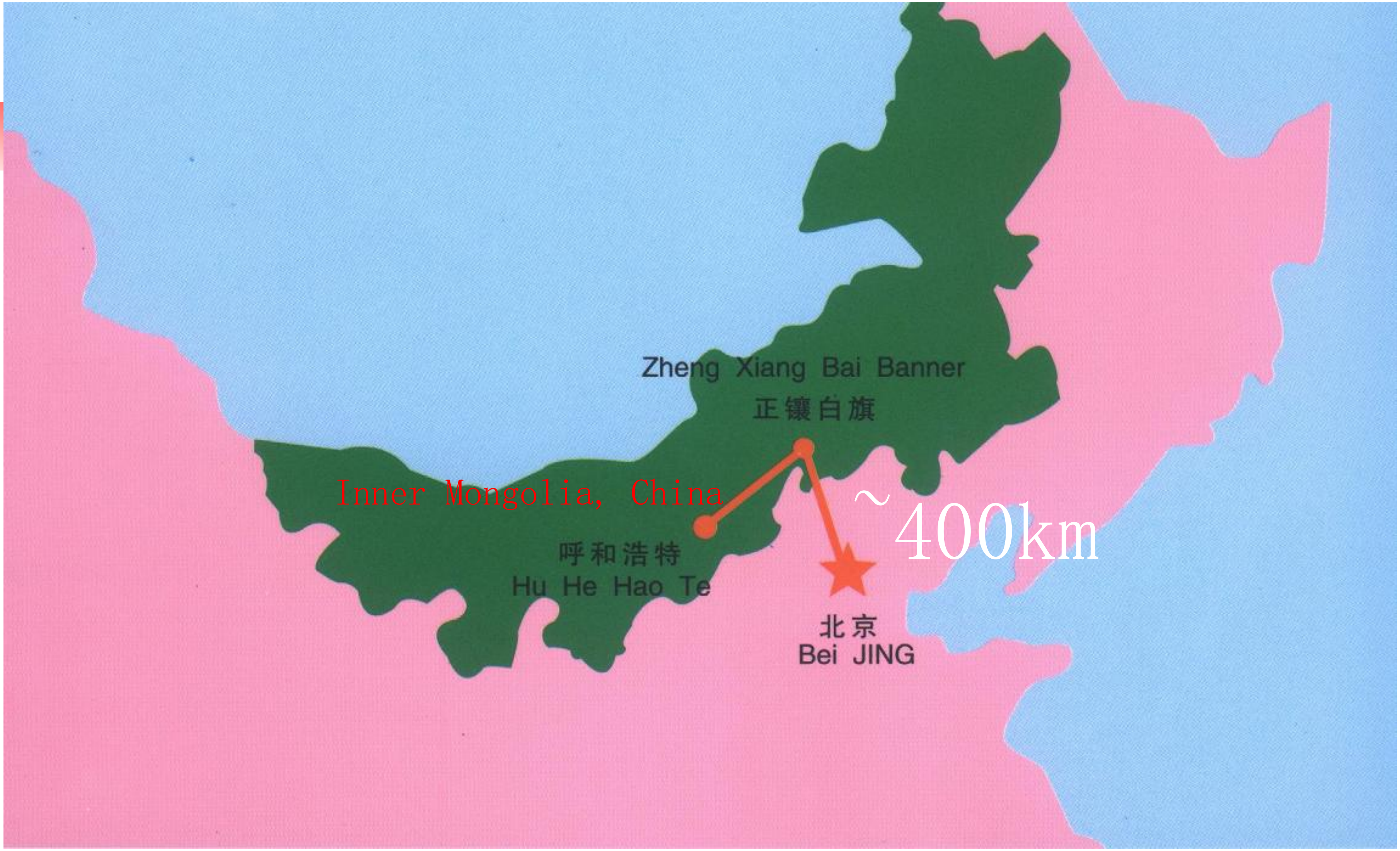

Site and Construction of CSRH

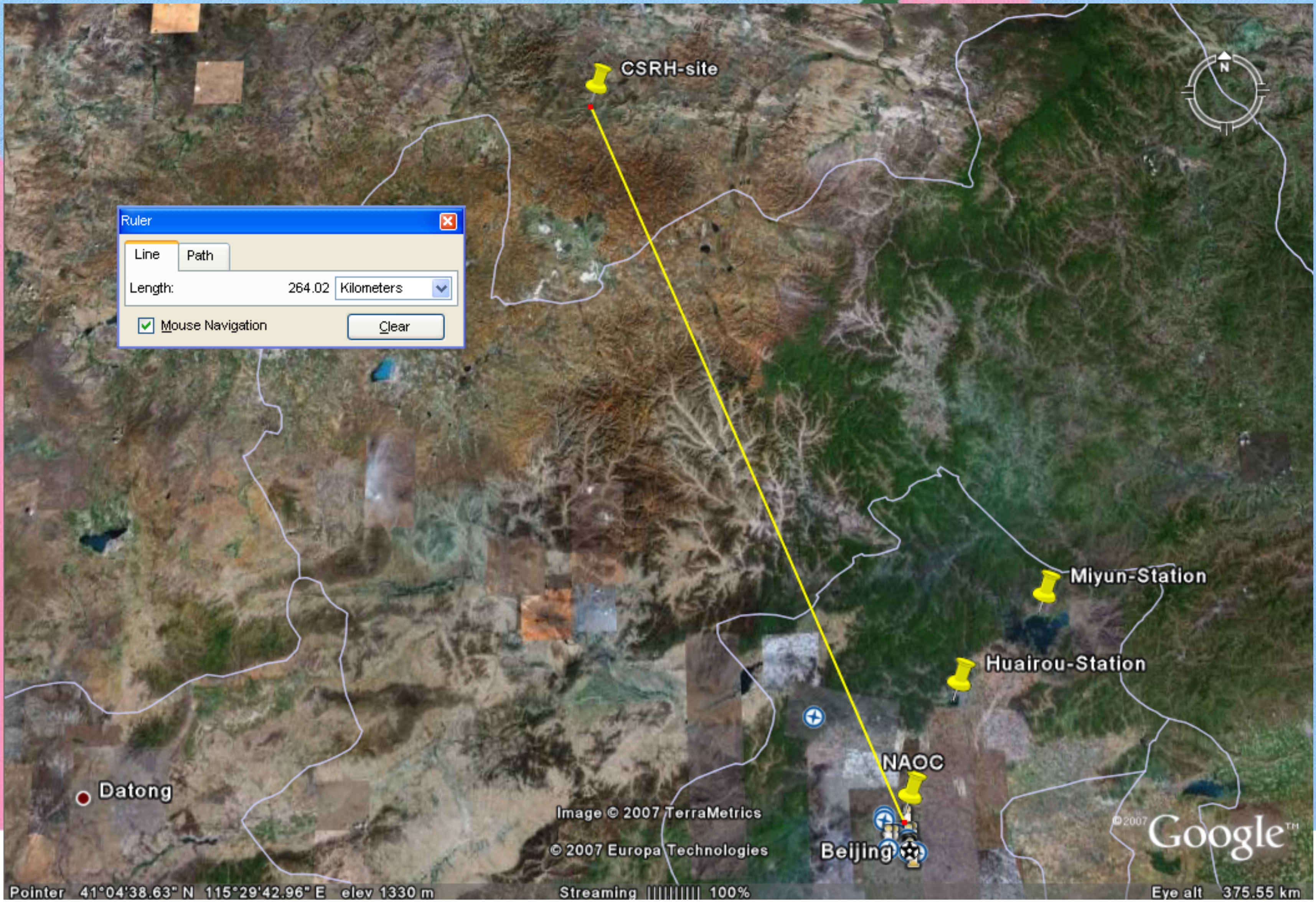

Site and Construction of CSRH

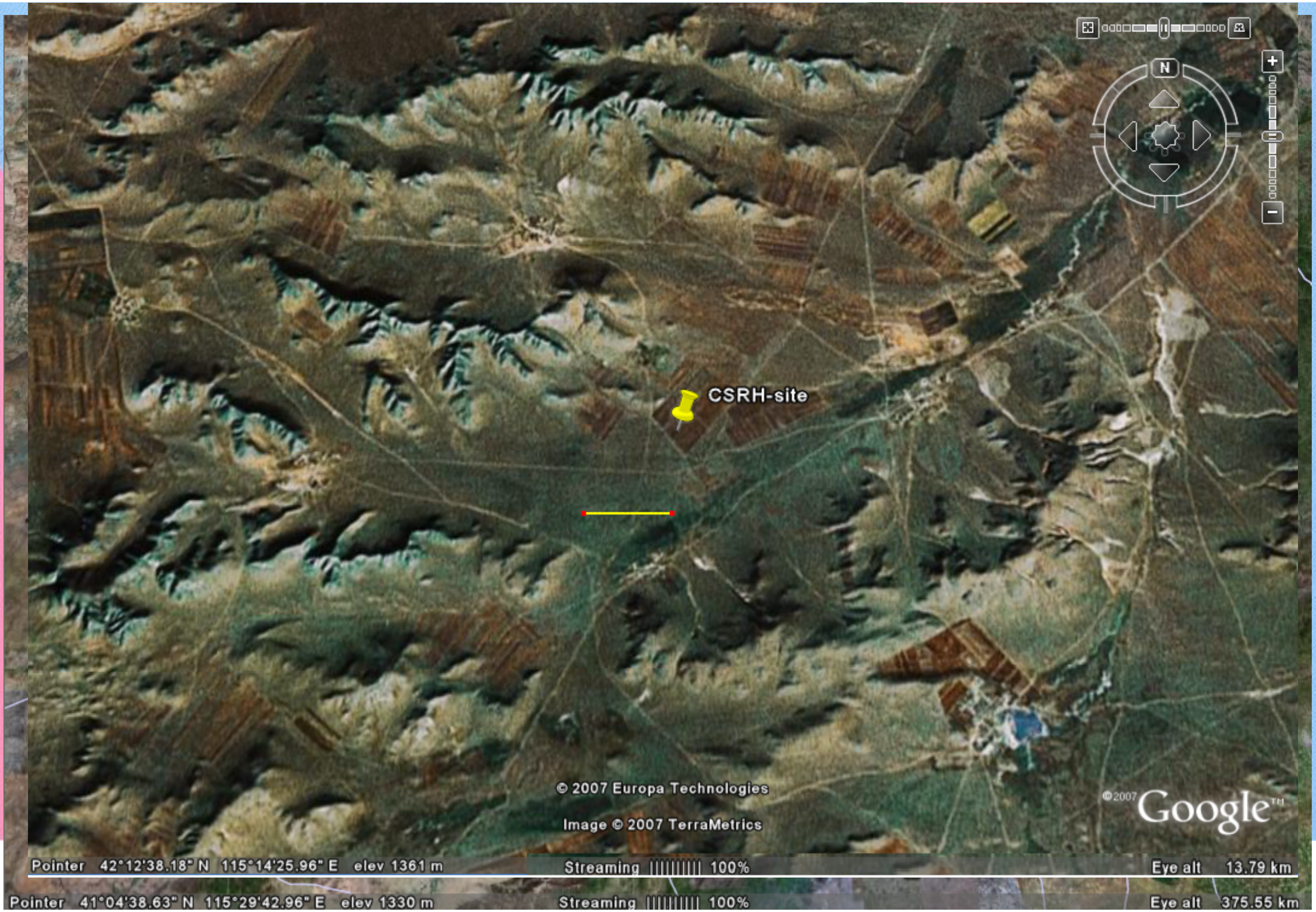

Ceremony for Construction of CSRH at Ming’antu Observatory on 9/9/2008

Array configuration (simulation):

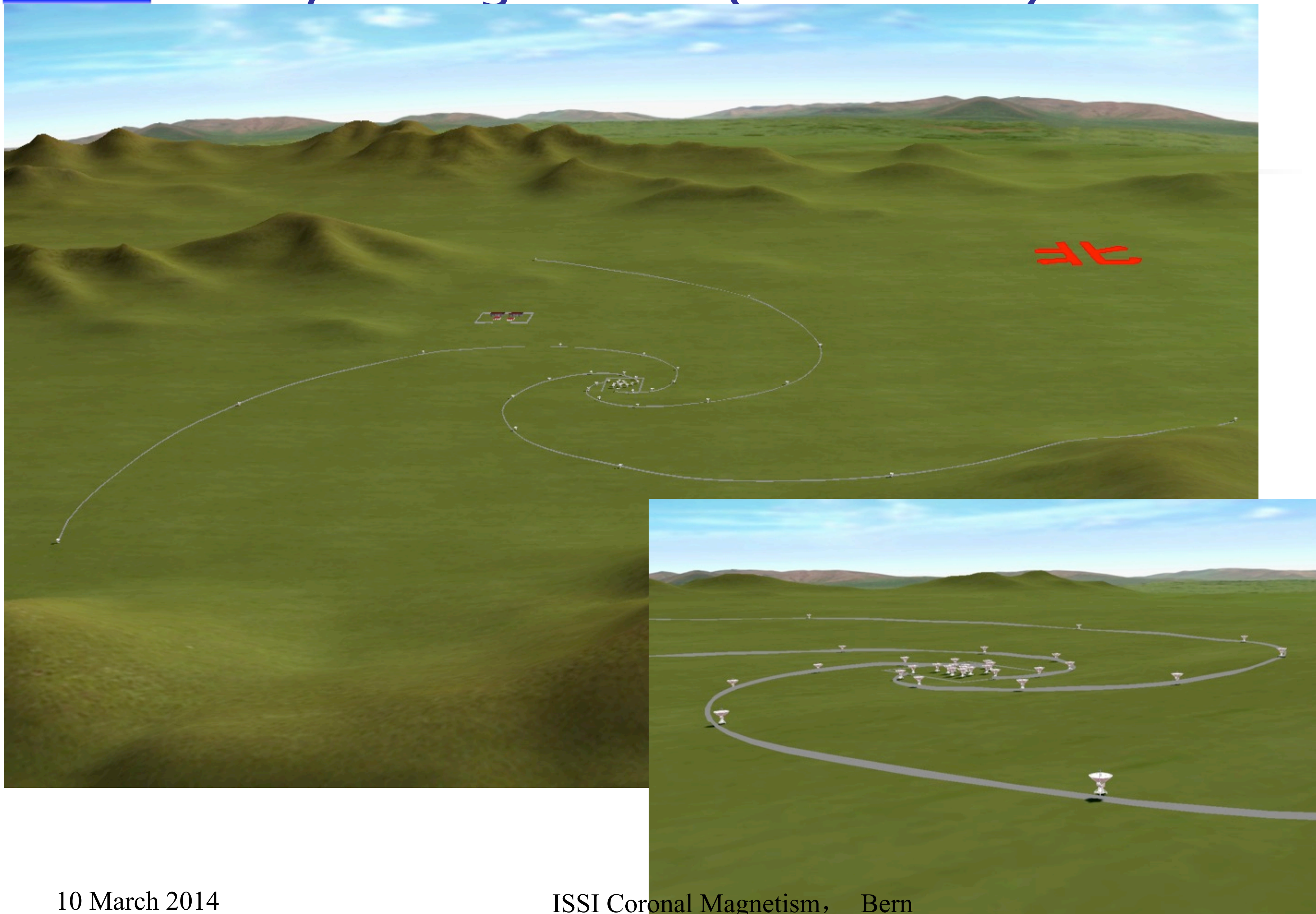

Array construction:

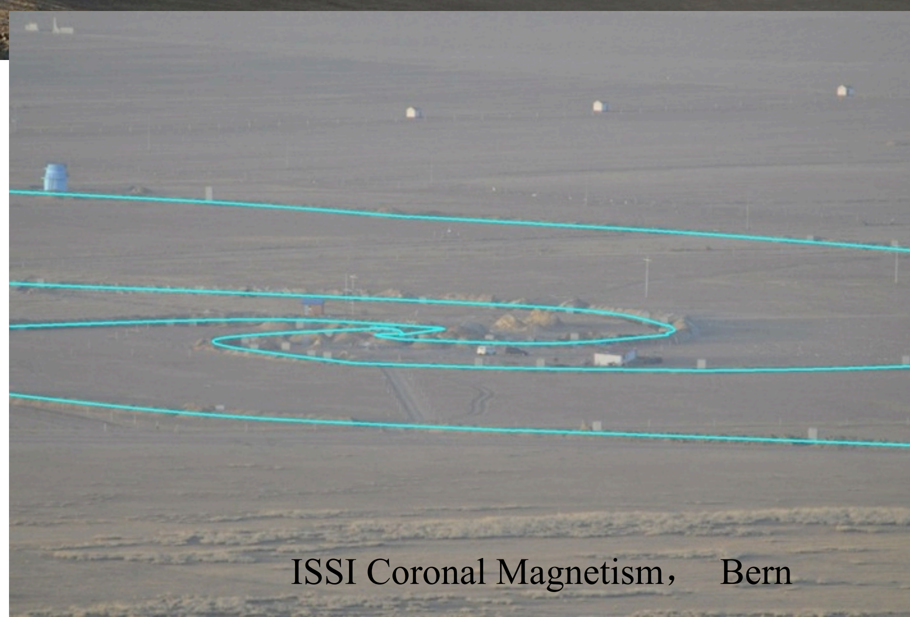

Optical fibers deployed

Array Construction

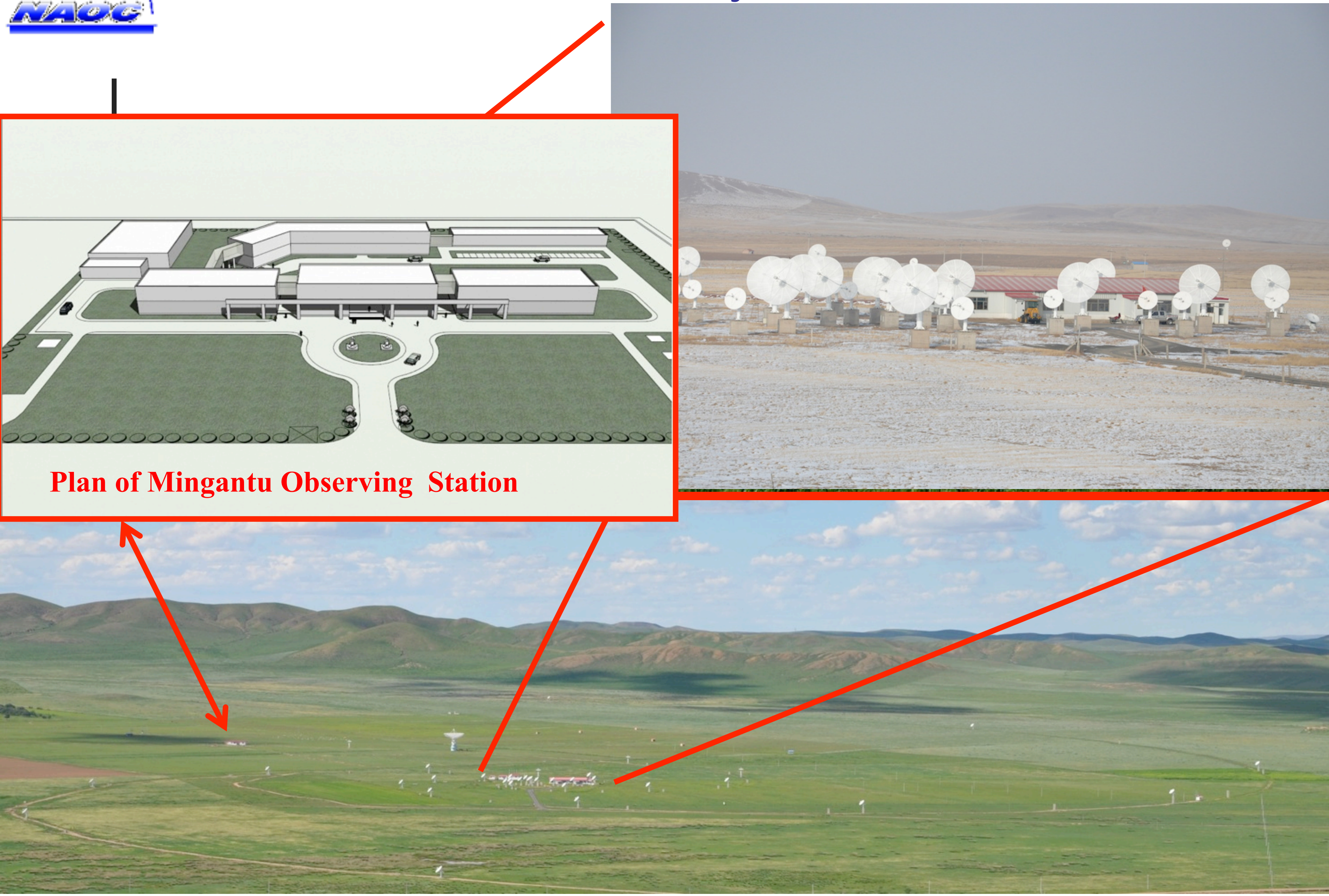

Indoor devices

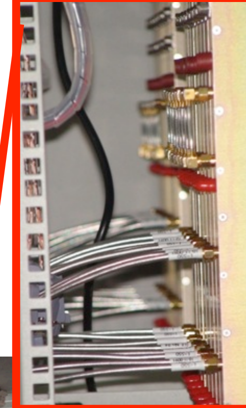

Back side view

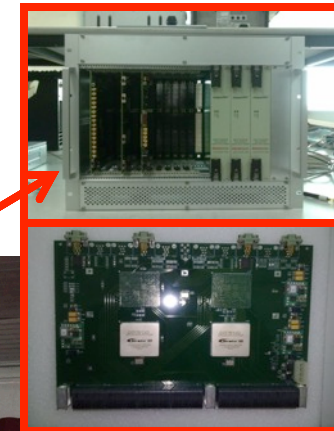

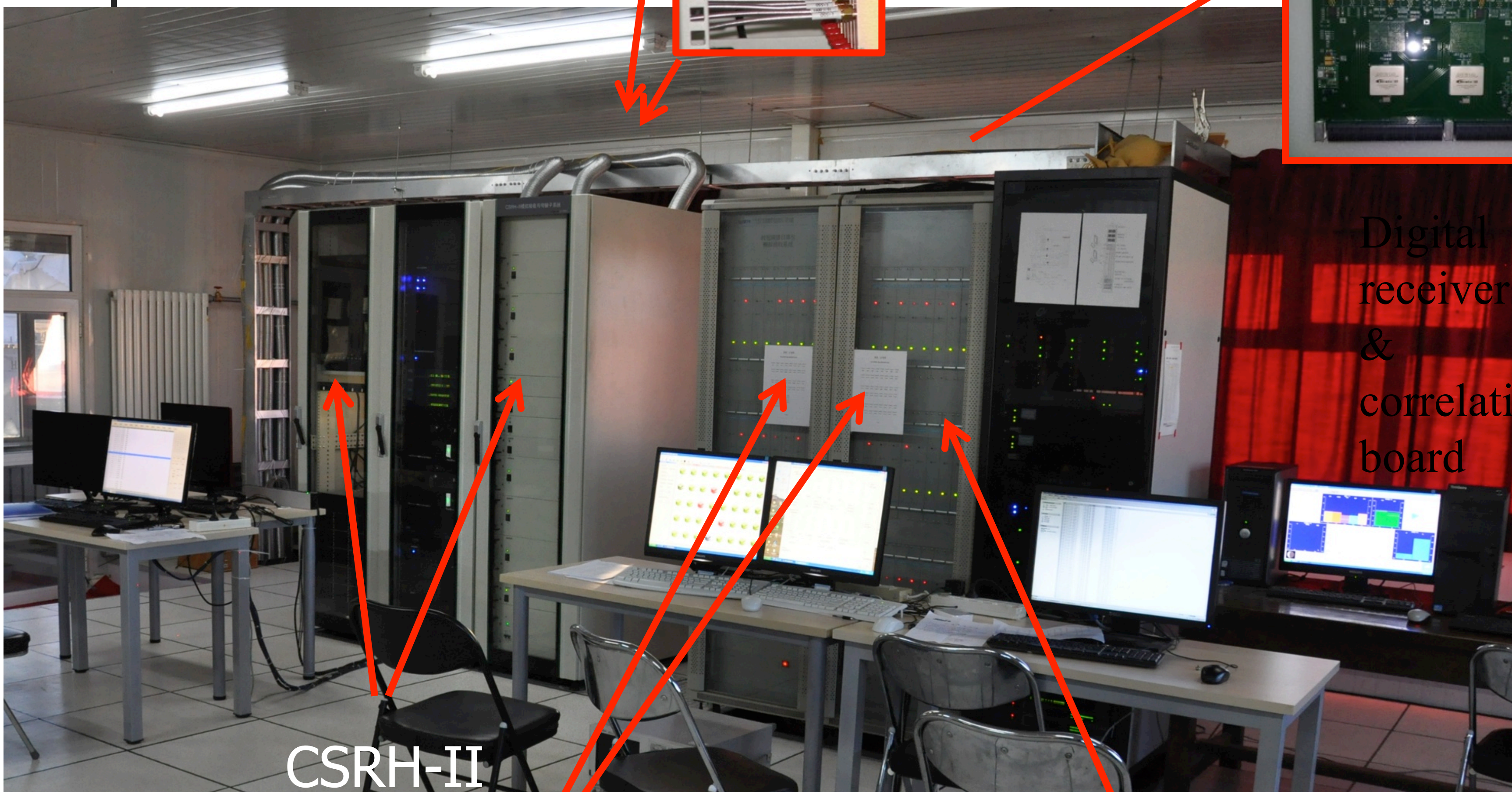

CSRH-I analog receivers and monitoring sub-system

CSRH-I in CASA

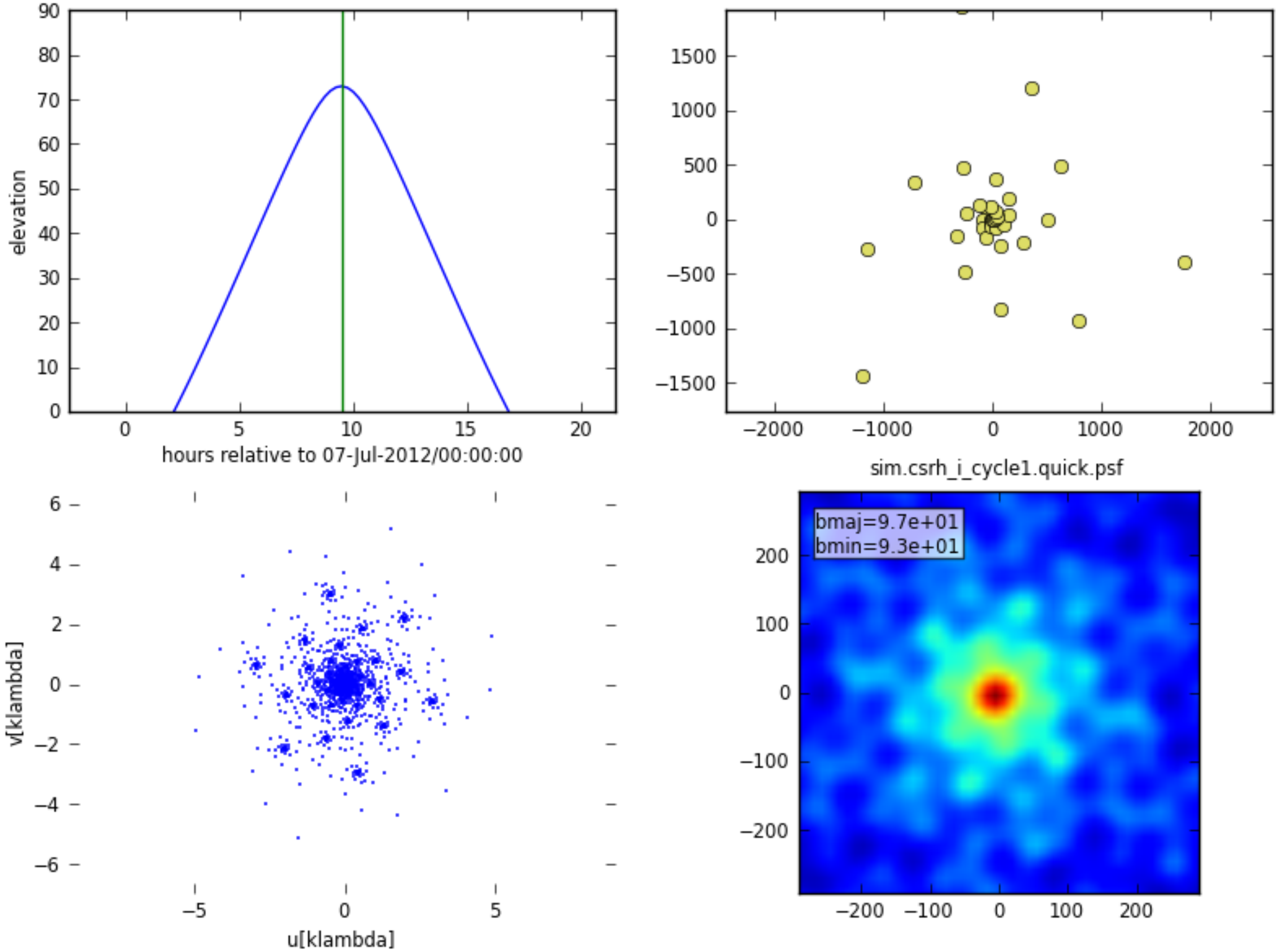

FY-2 satellite 1.7 GHz (CSRH Beam at 1.7GHz)
Up panel: FOV 1.7 deg， lower panel: FOV 12 arc min

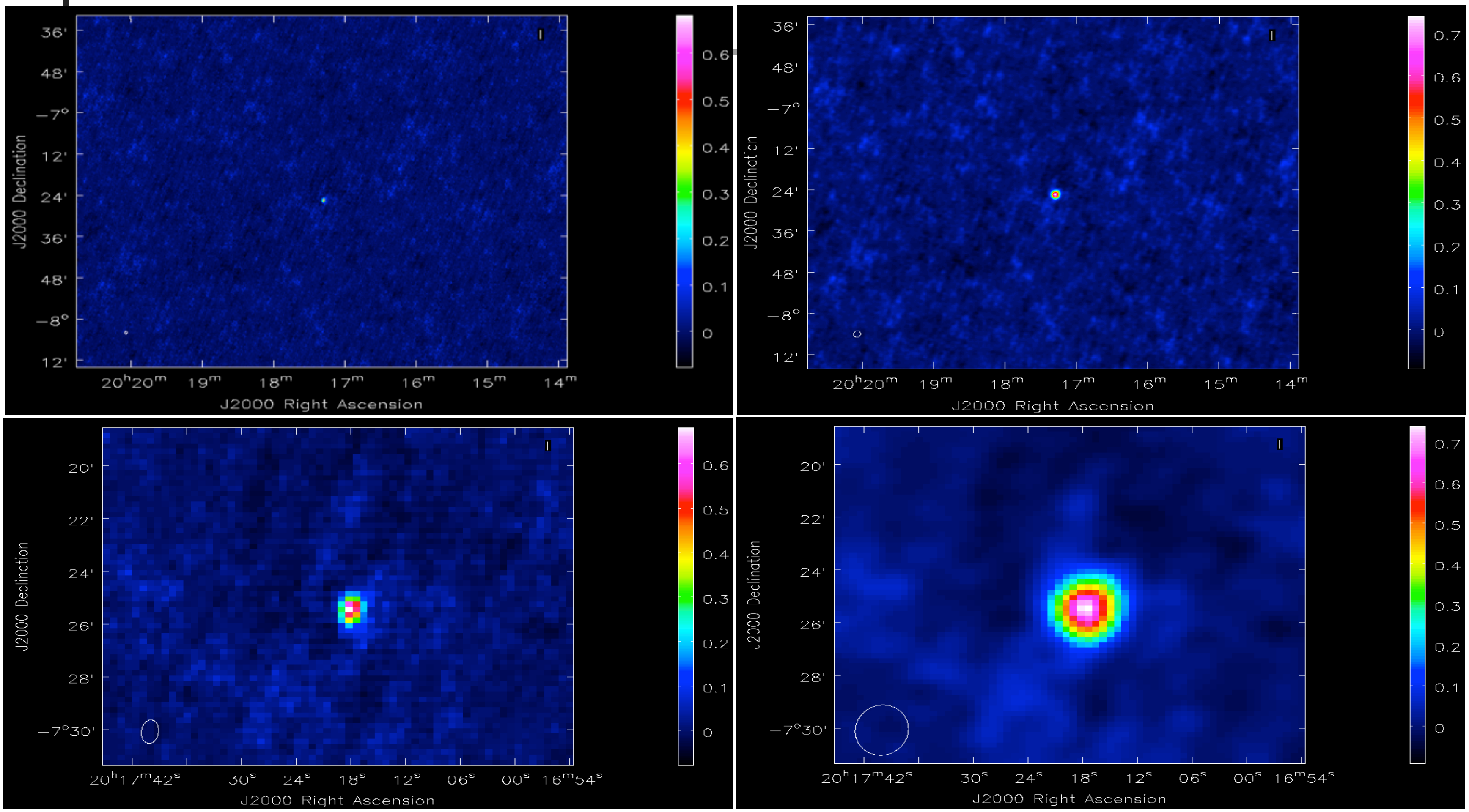

Test observations with CSRH-I

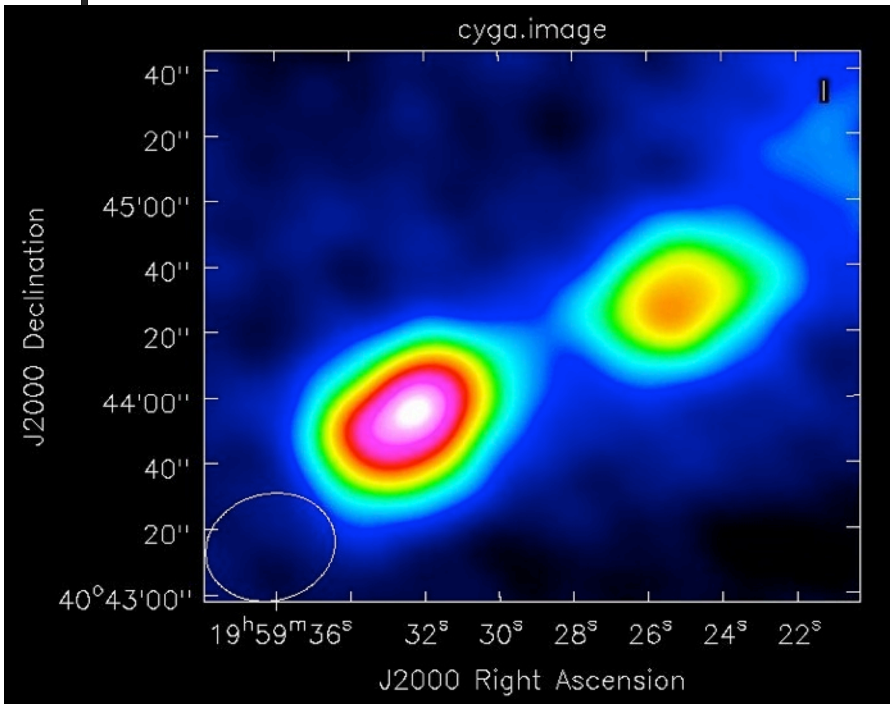

Test of Cyg A observed at 1.7 GHz on 5 Jun 2013 at 5:30 UT with 1s integral time.

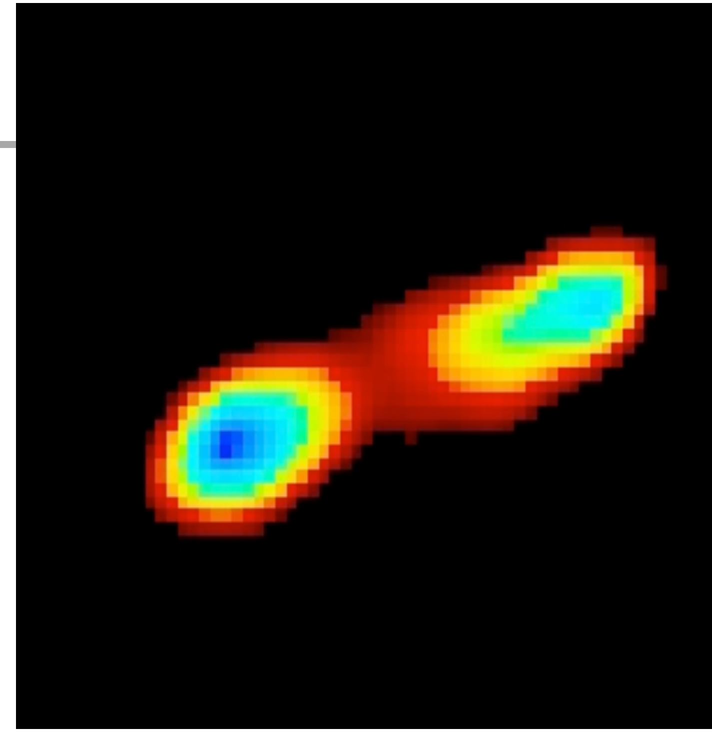

GMRT 610 MHz Image （not scaled, GMRT web）

CSRH-I image of the quiet Sun on 22 Jan 2014 (Development through CASA package)

Preliminary result with 60 ms integral time

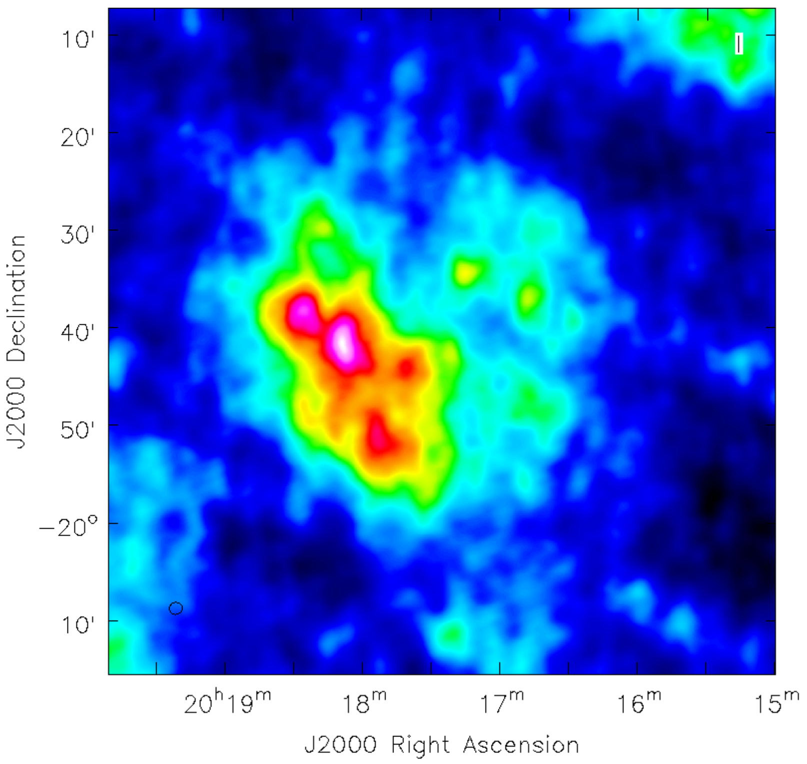

Dirty map

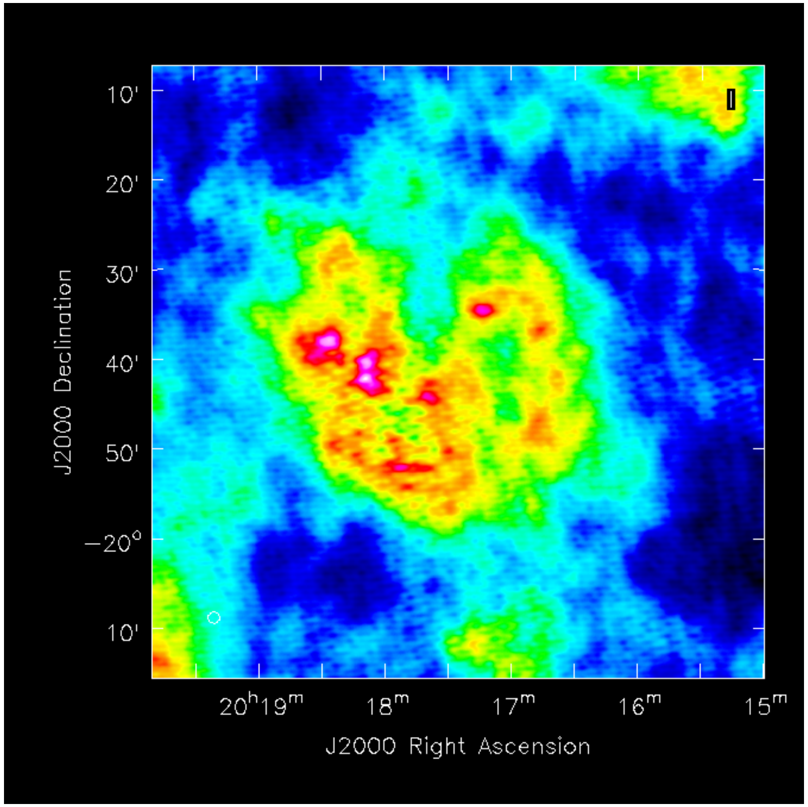

Cleaned map

CSRH-I image of the quiet Sun on 22 Jan 2014 (processed outside of the CASA package)

Preliminary result with 60 ms integral time

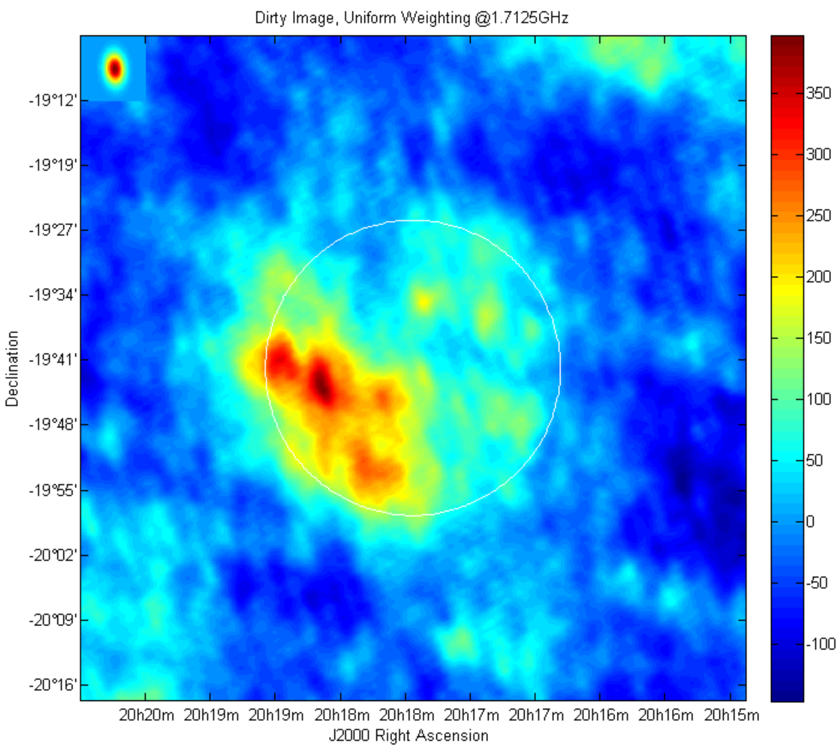

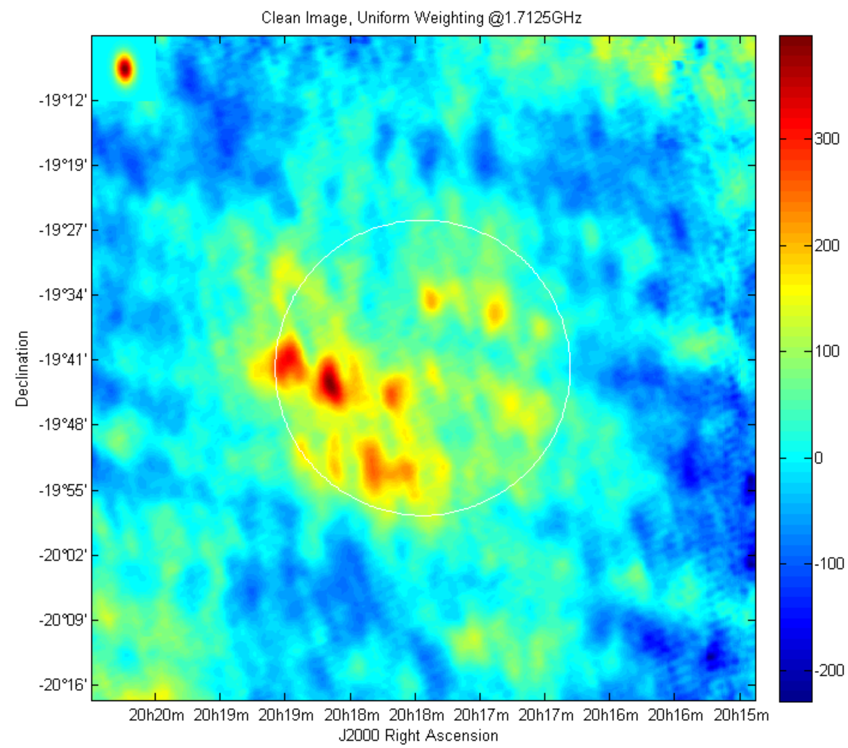

Dirty map with direct FT

Cleaned map

(The faint circle indicate optical size of the Sun with error ~arcmin due to uncertainty of the satellite position. Upleft corner shows the beam)

CSRH-I image of the quiet Sun on 22 Jan 2014 at 05:15:00 UT and comparison with other observations

Preliminary result with 60 ms integral time

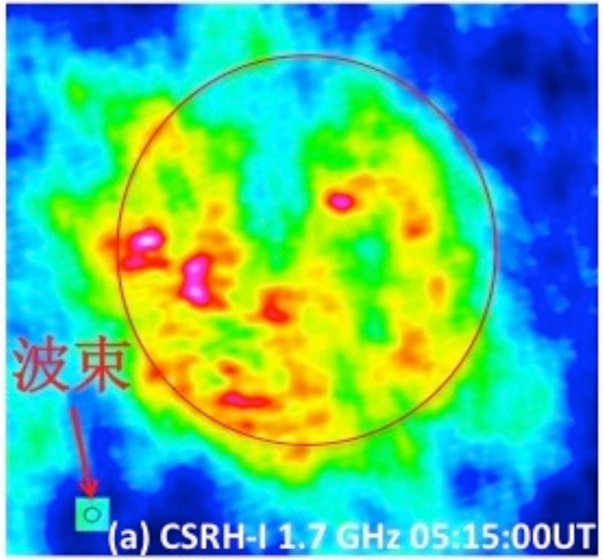

(a) CSRH-I 1.7 GHz 05:15:00UT

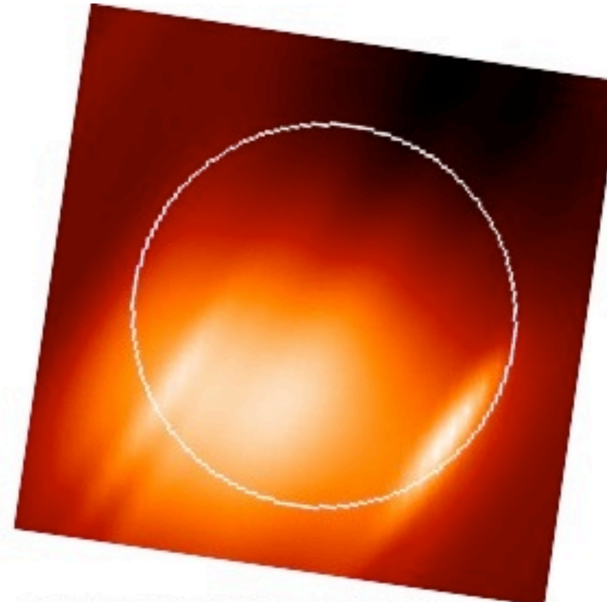
(b) NRH 432 MHz 08:46:02UT

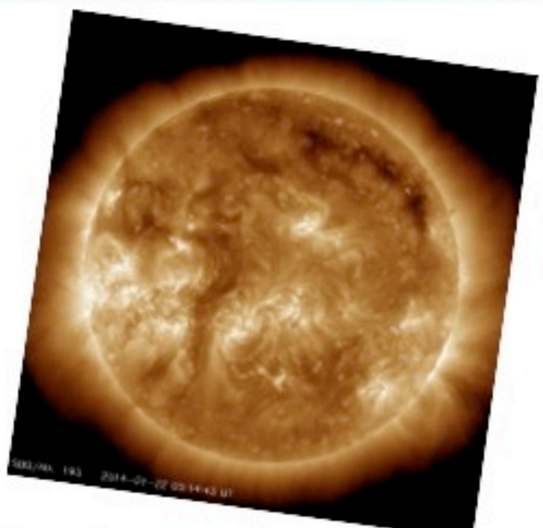
(c) AIA/SDO 193Å 05:14:43UT

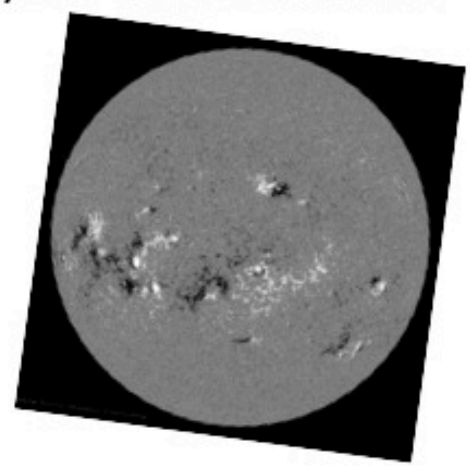
(d) HMI/SDO Bz 05:15:00UT

Pt-3 Summary

I. For CSRH, radio quiet zone protection is established:
   I. CSRH-I during 2008-2013:
   II. CSRH-II finished construction in 2013
II. Develop data pipe-line now
III. Mingantu Observing Station construction in 2014
IV. CSRH will provide imaging spectroscopic observations to determine flare onset regime and to obtain coronal magnetic field distributions.


Thanks
HA2
(Photo by S.J. Yu)

High Performance Feed Development

The available Eleven feed cannot meet the needs of solar observations as some parameters including VSWR, cross circular polarization degree are not with high performance.

E.g., Eleven Feed for SKA (Olsson,Kildal, Weinreb 2006, IEEE)

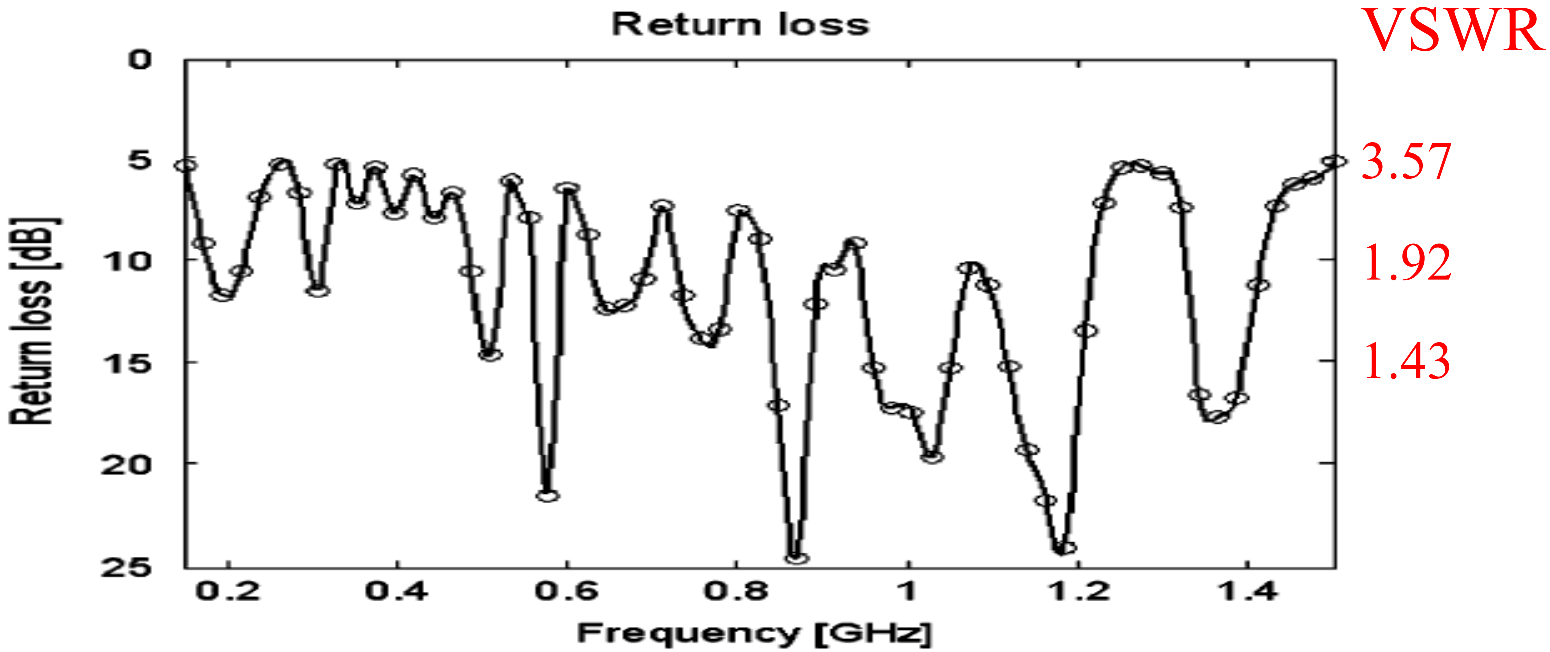

High Performance Feed Development

The available Eleven feed cannot meet the needs of solar observations as some parameters including VSWR, cross circular polarization degree are not with high performance.

E.g., Eleven Feed for SKA (Olsson,Kildal, Weinreb 2006, IEEE)

VSWR

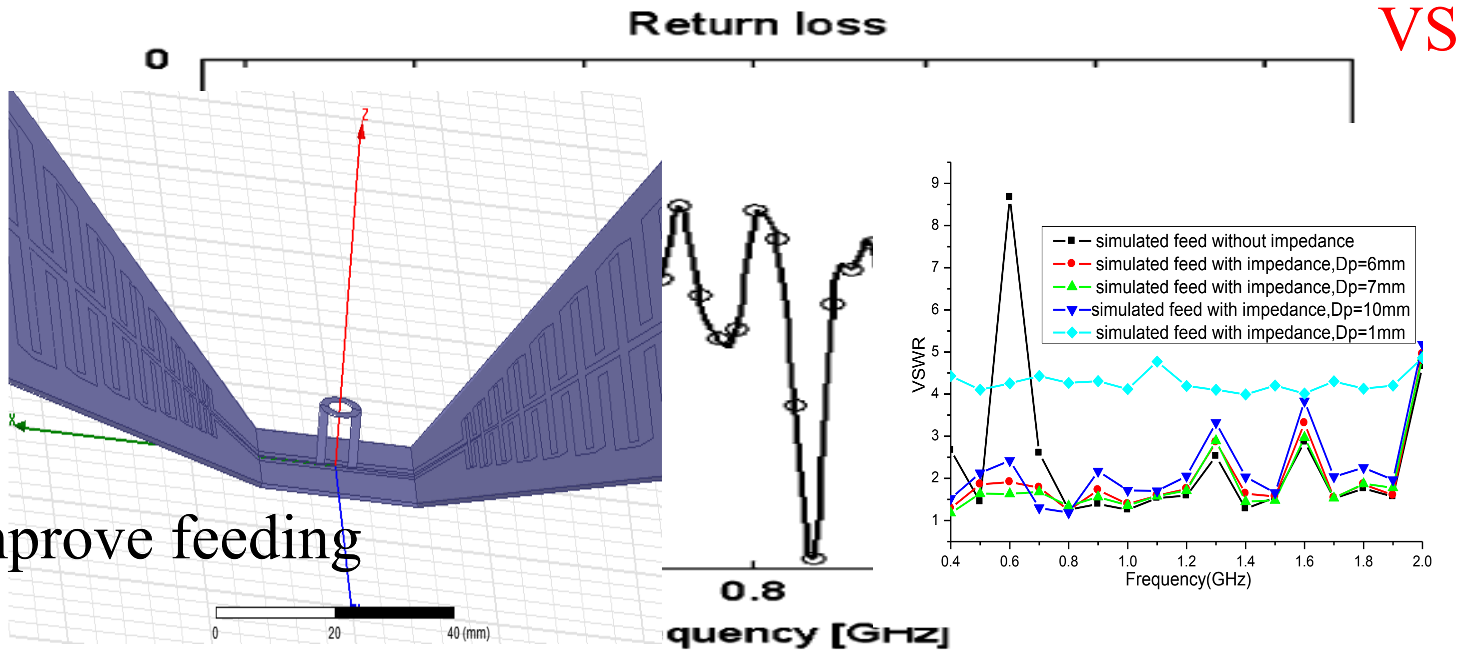

Test for high performance feed

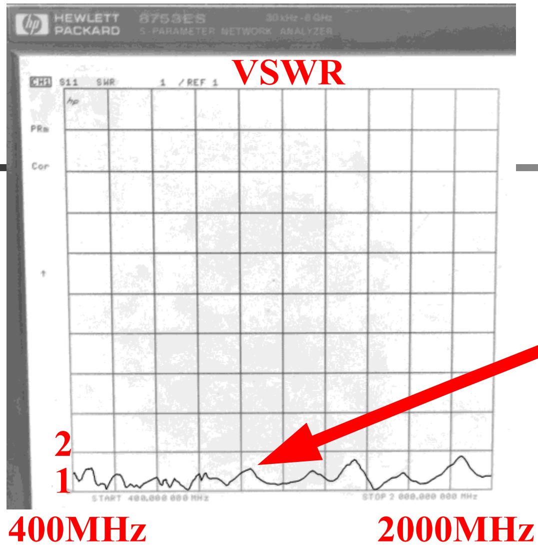

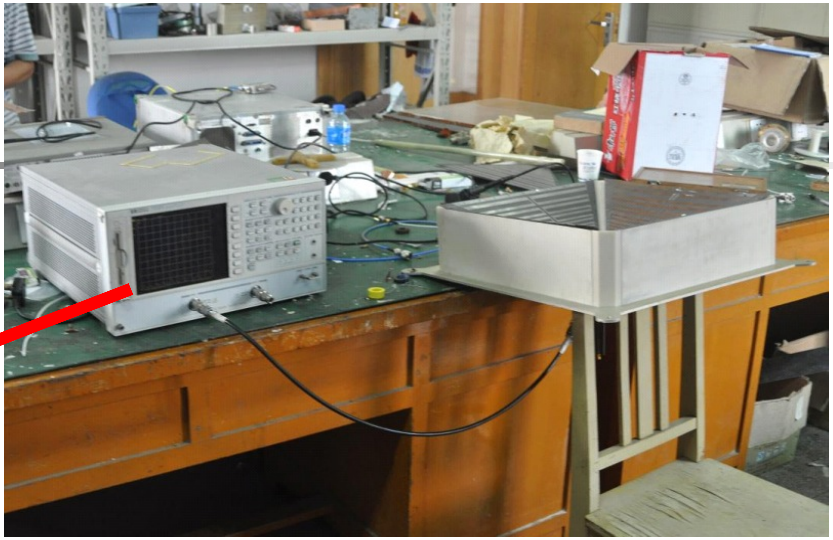

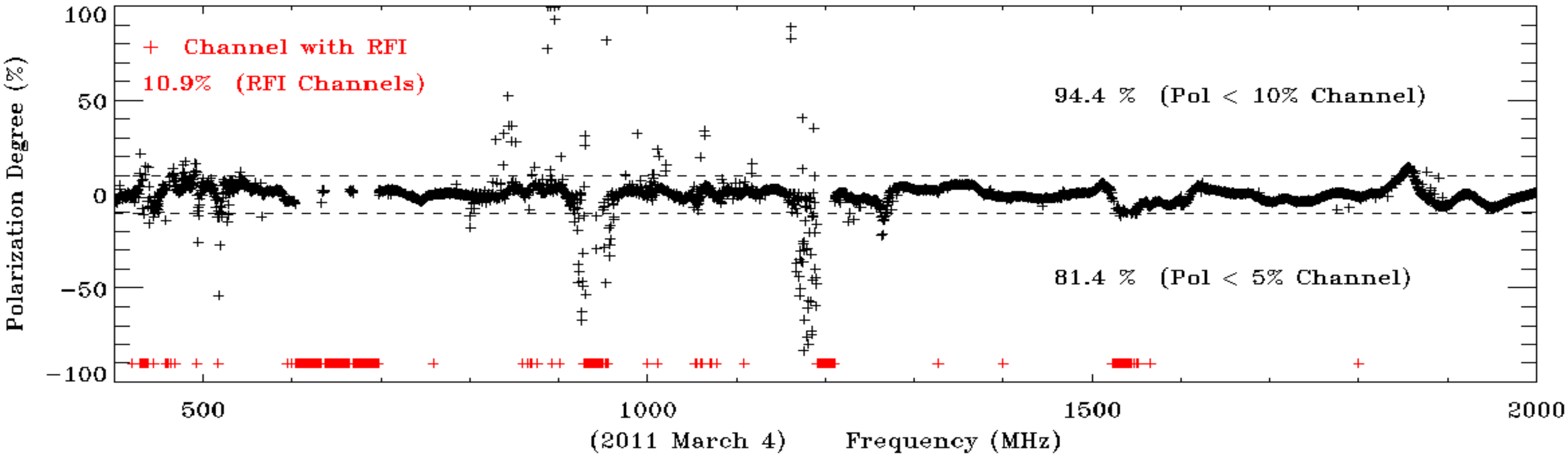

Test for high performance feed

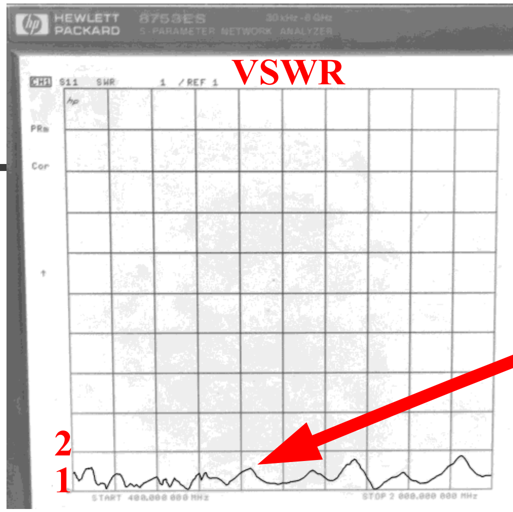

400MHz 2000MHz

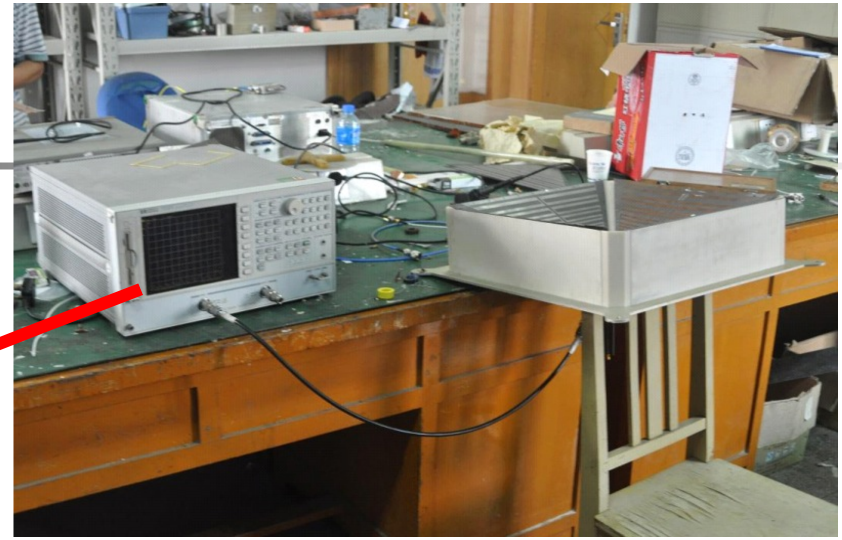

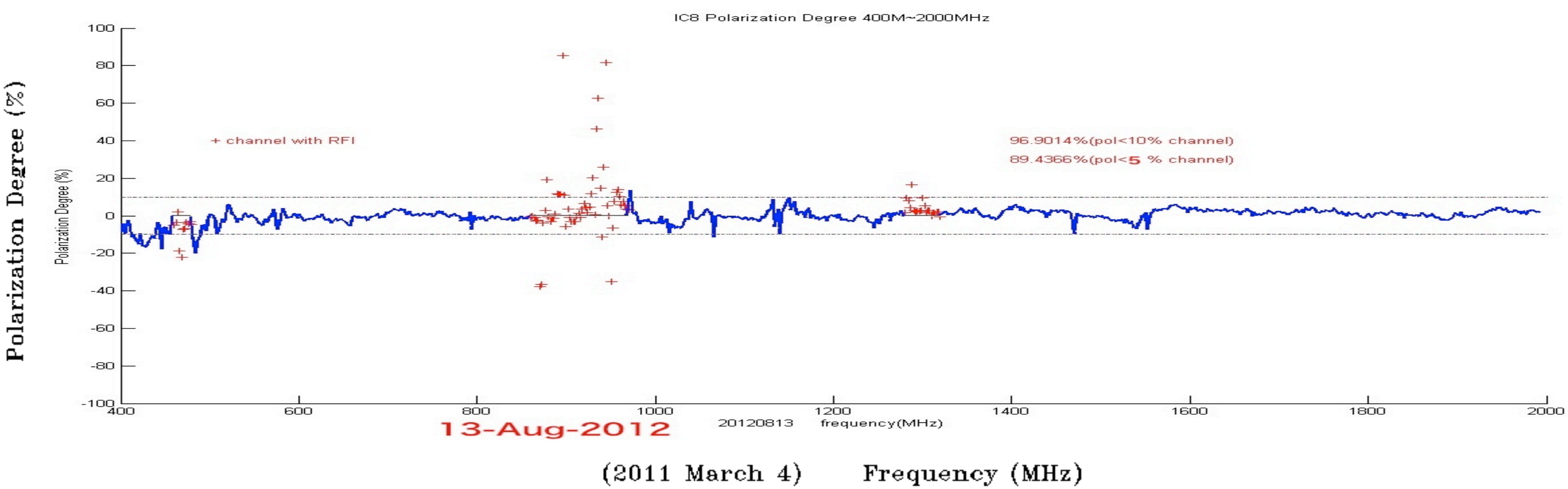

CSRH-I Band-Switching Stability: IF output Measurements: 3ms integral time at 25ms cycle

CSRH-I Band-Switching Stability: IF output Measurements: 3ms integral time at 25ms cycle

CSRH-I Band-Switching Stability: IF output Measurements: 3ms integral time at 25ms cycle

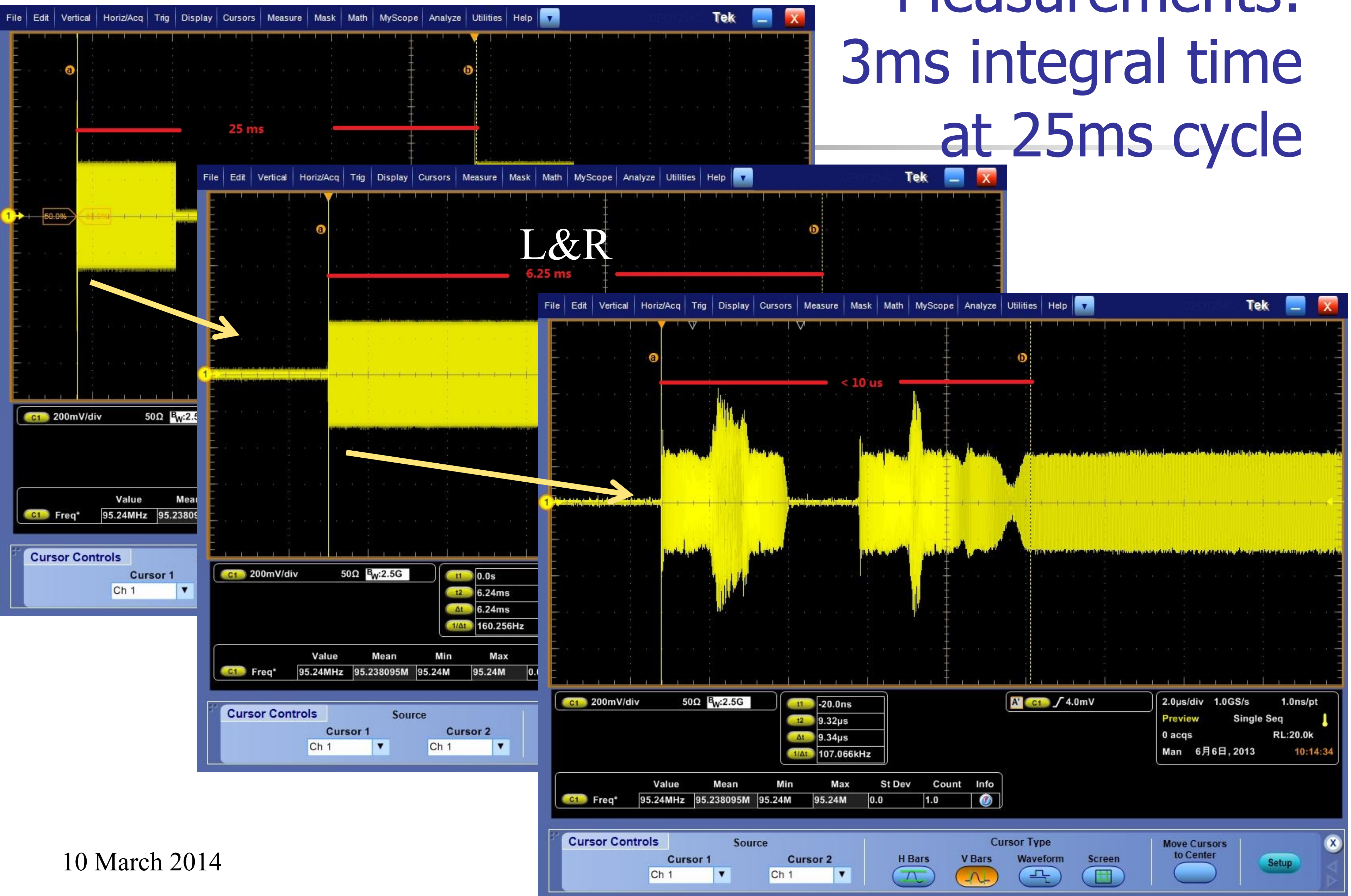

10 March 2014